RSC Advances

ROYAL SOCIETY OF CHEMISTRY

PAPER

View Article Online
View Journal | View Issue

Cite this: *RSC Adv.*, 2025, **15**, 40209

Rb_2BX_6 double perovskites: unlocking 22% efficiency through structural, electronic, mechanical, and optical insights

Imtiaz Ahamed Apon, [a] Karim KRIAA,[b] Md. Azizur Rahman, *[c] Md. Alamgir Hossain,[d] Chemseddine Maatki,[b] Amine Aymen Assadi[b] and Noureddine Elboughdiri [e]

Developing stable and efficient perovskite-inspired materials has become a key focus in the pursuit of next-generation solar energy technologies, with recent advances in material design highlighting the potential of novel halide structures as sustainable alternatives to conventional silicon-based solar absorbers. This study presents a comprehensive first-principles investigation of novel Rb-based double perovskites, Rb_2BX_6 (B = Sn/Pb; X = Cl/Br), highlighting their potential for photovoltaic applications. All compounds exhibit negative formation enthalpies, indicating thermodynamic stability, and tolerance factors around 0.80 confirm structural feasibility. Mechanical stability is validated through Born criteria and elastic constants. Band structure calculations reveal direct band gaps of 2.646 eV (Rb_2SnCl_6), 1.451 eV (Rb_2SnBr_6), 1.379 eV (Rb_2PbCl_6), and 0.357 eV (Rb_2PbBr_6), suggesting semiconducting behavior, with Rb_2SnBr_6 and Rb_2PbCl_6 falling within the optimal range for visible-light absorption. Partial density of states (PDOS) analyses show that the valence bands are mainly composed of halide p-orbitals, while conduction bands are dominated by B-site s- and p-orbitals. ELATE tensor analysis reveals moderate elastic anisotropy, with anisotropy indices of 0.22 for Rb_2SnBr_6 and 0.18 for Rb_2PbCl_6. Optical studies indicate absorption coefficients exceeding 10^5 cm^{-1} in the visible region for both materials. Mulliken population analysis confirms strong ionic bonding and moderate charge transfer between atoms. Moreover, Rb_2SnCl_6 and Rb_2PbCl_6 are dynamically stable, whereas Rb_2SnBr_6 and Rb_2PbBr_6 exhibit dynamic instability. SCAPS-1D device simulations yield a power conversion efficiency (PCE) of 20.44% for Rb_2SnBr_6, accompanied by a short-circuit current density (J_{SC}) of 22.3 mA cm^{-2}, an open-circuit voltage (V_{OC}) of 1.01 V, and a fill factor (FF) of 89.7%. For Rb_2PbCl_6, a slightly higher PCE of 21.84% is achieved (J_{SC} of 23.1 mA cm^{-2}, V_{OC} of 1.05 V, FF of 90.1%). Although Rb_2PbCl_6 demonstrates superior efficiency, its toxicity due to lead content poses environmental concerns. In contrast, Rb_2SnBr_6 offers a highly efficient, non-toxic alternative, positioning it as a viable candidate for eco-friendly and sustainable photovoltaic devices.

Received 5th June 2025
Accepted 14th October 2025

DOI: 10.1039/d5ra03981a

rsc.li/rsc-advances

1 Introduction

The family of A_2BX_6 halide double perovskites, also known as vacancy-ordered double perovskites, has a research lineage that spans nearly a century.[1] These compounds were first reported in the early 20th century in the context of solid-state inorganic chemistry, where they were synthesized as stable derivatives of the conventional ABX_3 perovskite lattice.[2] The defining structural feature of A_2BX_6 phases is the removal of every second B-site cation, leading to a rock-salt ordering of BX_6 octahedra separated by isolated vacancies. This ordered vacancy arrangement was systematically classified by Pauling and others in the 1920s to 1930s, and subsequent crystallographic investigations established the cubic fluorite-related framework as their characteristic.[3] Initially, these halide double perovskites were studied primarily for their structural chemistry and thermodynamic stability rather than for functional applications.

The renewed interest in A_2BX_6 perovskites arose after the success of lead halide perovskite solar cells post-2009.[4,5] Among them, rubidium-based double perovskites (Rb_2BX_6) exhibit structural robustness, optimal band gaps, and superior electronic properties, making them promising candidates for optoelectronic and photovoltaic applications.[6–8] Tin (Sn)-based and lead (Pb)-based double halide perovskites, particularly

[a]*Department of Electrical and Electronic Engineering, Bangladesh Army University of Science and Technology (BAUST), Saidpur-5311, Bangladesh*
[b]*Imam Mohammad Ibn Saud Islamic University (IMSIU), Riyadh 11432, Saudi Arabia*
[c]*Department of Electrical and Electronic Engineering, Begum Rokeya University, Rangpur, 5400, Bangladesh. E-mail: azizurrahmanatik49@gmail.com*
[d]*Department of Physics, Khulna University of Engineering & Technology (KUET), Khulna-9203, Bangladesh*
[e]*Chemical Engineering Department, College of Engineering, University of Ha'il, P.O. Box 2440, Ha'il 81441, Saudi Arabia*

Rb_2SnX_6 (X = Cl, Br), have garnered increasing attention for their tunable band gaps, strong visible-light absorption, and enhanced stability.[9,10] Pb-halide perovskites have emerged as one of the most promising classes of semiconductors, primarily because of their band gap tunability, efficient charge transport, and outstanding photoluminescence quantum yield (PLQY), which together underpin their success in photovoltaic and light-emitting applications.[11–13] However, their environmental concerns have shifted research toward Sn-based alternatives.[14] Density Functional Theory (DFT) calculations and experimental studies have validated the thermodynamic stability and suitable band gaps (0.9 to 0.6 eV) of Sn-based double perovskites, confirming their potential for high-performance solar cells.[15–17]

Recent studies have further highlighted the promise of Sn-based perovskites. Faizan *et al.* investigated A_2BX_6 (A = Rb, Cs; B = Sn, Pd, Pt = Cl, Br, I) using DFT, revealing strong dielectric constants and superior light absorption, critical for efficient energy conversion.[18] Karim *et al.* synthesized and characterized Cs_2SnX_6 (X = Cl, Br, I), reporting optical band gaps ranging from 4.89 eV (Cs_2SnCl_6) to 1.35 eV (Cs_2SnI_6), with mixed halide systems exhibiting non-linear optical behavior due to symmetry distortions.[19] Vamsi Krishna *et al.* conducted DFT studies on A_2BX_6 (A = Cs; B = Sn; X = Cl, Br, I) perovskites, confirming their strong potential for single- and multi-junction solar cells.[20] The synergy between theoretical and experimental approaches is crucial for advancing the optoelectronic, thermoelectric, and photocatalytic applications of these materials. Double perovskites are commonly synthesized using solution-based methods or solid-state reactions, with experimental studies confirming wide band gaps, such as 2.97 eV for Rb_2SnBr_6.[21] There are many other studies on A_2BX_6 compounds that have previously demonstrated promising efficiencies for photovoltaic applications. Such as according to K. Bouferrache *et al.*, the lattice constants of Cs_2MCl_6 (M = Se, Sn, Te, Ti) agree with experiments within 1.3 to 3%. Cs_2SnCl_6 is isotropic, while the others are anisotropic, especially Cs_2TiCl_6. Their low elastic moduli indicate they are easily deformable.[22] Rifat *et al.* reported that K_2CeCl_6-based solar cells achieved 17.22% PCE, 1.02 V_{OC}, 22.5 mA cm^{-2} J_{SC}, and ~81% FF.[23] Md. S. H. Saikot *et al.* reported that Na_2PdCl_6-based solar cells achieved 25.55% PCE (J_{SC} 42.55 mA cm^{-2}, V_{OC} 0.758 V, FF 79.16%), outperforming Li_2PdCl_6 with 23.06% PCE (J_{SC} 38.12 mA cm^{-2}, V_{OC} 0.786 V, FF 76.97%).[24]

This study employs first-principles calculations to systematically investigate the structural, electronic, optical, mechanical, phonon, and charge population properties of Rb_2SnCl_6, Rb_2SnBr_6, Rb_2PbCl_6, and Rb_2PbBr_6. The effects of absorber layer thickness, defect density, and other key parameters on overall solar cell performance are also evaluated through device-level simulations. By examining the influence of cation substitution (Sn *vs.* Pb) and halide variation (Cl *vs.* Br), detailed insights are provided into their suitability for optoelectronic and energy-harvesting applications. This work provides a comprehensive theoretical framework linking fundamental material properties to device-level performance, paving the way for the design of efficient and environmentally sustainable perovskite solar absorbers.

2 Computational method

All density functional theory (DFT) calculations were performed with the plane-wave pseudopotential code CASTEP (Cambridge Sequential Total Energy Package) of Materials Studio (MS) software.[25,26] Norm-conserving pseudopotentials (NCPP) were used for all elements. A plane-wave kinetic energy cutoff of 800 eV, determined from convergence tests, was applied throughout the calculations. Self-consistent field (SCF) iterations were performed with an energy tolerance of 5.0×10^{-7} eV and a maximum of 100 cycles. Additionally, crystal structures were visualized using VESTA.[27] Brillouin-zone integrations employed Monkhorst–Pack meshes,[28] with a $6 \times 6 \times 6$ grid for geometry optimization and a denser $12 \times 12 \times 12$ grid for non-self-consistent (NSCF) calculations of the density of states (DOS) and optical spectra. The total energy convergence criterion was set to 1×10^{-8} eV per atom, while structural relaxations were carried out until the maximum Hellmann–Feynman force on any atom was below 0.01 eV $Å^{-1}$ and the residual stress components were less than 0.02 GPa. Exchange–correlation effects were treated using a tiered approach to balance accuracy and computational cost. Geometry optimizations and initial electronic structure scans were carried out with the generalized gradient approximation of Perdew–Burke–Ernzerhof (GGA-PBE).[29] Unless otherwise specified, the reported electronic, mechanical, optical, and charge-population properties are presented at the GGA-PBE level for consistency and efficiency. Hybrid functionals such as HSE06 were employed selectively to validate key results, particularly band gap values and structural parameters, but were not used for all subsequent property evaluations.[30,31] Optical properties were calculated within the independent-particle approximation using PBE eigenvalues and wavefunctions on a $12 \times 12 \times 12$ k-point grid. A Gaussian broadening of 0.05 eV was applied to obtain smooth spectra. Elastic constants C_{ij} were determined using the finite-strain method implemented in CASTEP, while macroscopic elastic moduli were derived *via* the Voigt–Reuss–Hill average. Elastic anisotropy was visualized using the ELATE tool.[32] Charge analyses (Mulliken, Hirshfeld, and where noted, Bader) were performed from the converged charge densities as implemented in CASTEP (see SI for details).[33] SCAPS-1D simulations of device performance[34,35] used DFT-derived absorber inputs (band gap from GGA-PBE, absorption coefficient, and DOS-derived effective masses).[36] The SCAPS device architecture and all input parameters are given in Tables 5 and 6.[37] The final illustrations were refined using Adobe Illustrator for enhanced graphical clarity and presentation of the solar cell devices.[38] These computational approaches provide a robust framework for accurately predicting the structural, electronic, and optical properties of the studied materials, ensuring the reliability of the subsequent analyses presented in this work.

3 Results and discussion

3.1 Structural properties

Investigating the structural properties of the Rb_2BX_6 (B = Sn/Pb, X = Cl/Br) double perovskites is a vital step in the DFT

simulation process, as it serves as the foundation for analyzing other physical characteristics, such as electrical and optical properties. In this study, the structural features of Rb_2BX_6 were examined using the GGA-PBE and hybrid-HSE06 approximations within the cubic fluorite structure space group $Fm\bar{3}m$ (#225).[39,40] Fig. 1a and b illustrates the primitive crystalline unit cell of Rb_2SnX_6 and Rb_2PbX_6 double perovskite materials.

In these structures, the Rb atom occupies the 8*c* Wyckoff position with fractional coordinates (0.25, 0.25, 0.25), while the Sn/Pb atom is positioned at the 4*a* Wyckoff site with coordinates (0, 0, 0). The X atom is located at the 24*e* Wyckoff site with fractional coordinates (0.244, 0, 0).[41,42] Additionally, Fig. 1c and d presents the schematic designs of solar cell architectures based on Rb_2SnBr_6 and Rb_2PbCl_6, highlighting their potential use as absorber layers in photovoltaic applications. This structural analysis provides a foundation for further exploration of their electronic, mechanical, and optical properties.

The Birch–Murnaghan equation of state (see eqn (1))[43] was applied to obtain the optimized volume and lattice parameters of the studied perovskite compounds.

$$E(V) = E_0 + \frac{B}{B'\left(B'-1\right)}\left[V\left(\frac{V_0}{V}\right)^{B'} - V_0\right] + \frac{B}{B'}(V - V_0) \quad (1)$$

To enhance the reliability of our predictions, four exchange–correlation functionals—GGA-PBE, GGA-PBEsol, *m*-GGA, and HSE06—were employed. GGA-PBE served as the baseline due to its wide adoption in structural and electronic studies, while PBEsol was included for its improved accuracy in describing equilibrium lattice parameters.[44] The *meta*-GGA functional was considered for its refined density-gradient corrections, and HSE06 was applied selectively to validate key electronic and structural properties.[45] The calculated lattice constants (Å) for Rb_2SnCl_6, Rb_2SnBr_6, Rb_2PbCl_6, and Rb_2PbBr_6 are 7.581, 7.933, 7.697, and 8.130 with GGA-PBE; 7.320, 7.605, 7.697, and 7.437 with GGA-PBEsol; 7.581, 7.932, 7.697, and 8.129 with HSE06; and 7.581, 7.932, 7.697, and 7.678 with *m*-GGA. The corresponding unit cell volumes ($Å^3$) are 308.174, 353.036, 322.443, and 354.245 with GGA-PBE; 275.548, 308.369, 293.009, and 326.250 with GGA-PBEsol; 274.806, 351.806, 291.031, and 381.810 with *m*-GGA; and 308.145, 352.497, 322.462, and 354.285 with HSE06. The observed variation in lattice constants and volumes reflects the intrinsic characteristics of the different functionals. GGA-PBE tends to overestimate lattice dimensions due to its underbinding nature, whereas PBEsol systematically underestimates them. The *m*-GGA functional generally yields intermediate values but can show larger fluctuations depending on bonding environments.[46] HSE06, which incorporates a fraction of exact exchange, provides improved electronic accuracy while maintaining structural parameters close to PBE. These systematic differences are consistent with previous benchmark studies and confirm that, despite numerical variations, the overall structural trends remain robust. These values are in good agreement with previous theoretical and experimental reports. For instance, the lattice constant of Rb_2SnBr_6 was

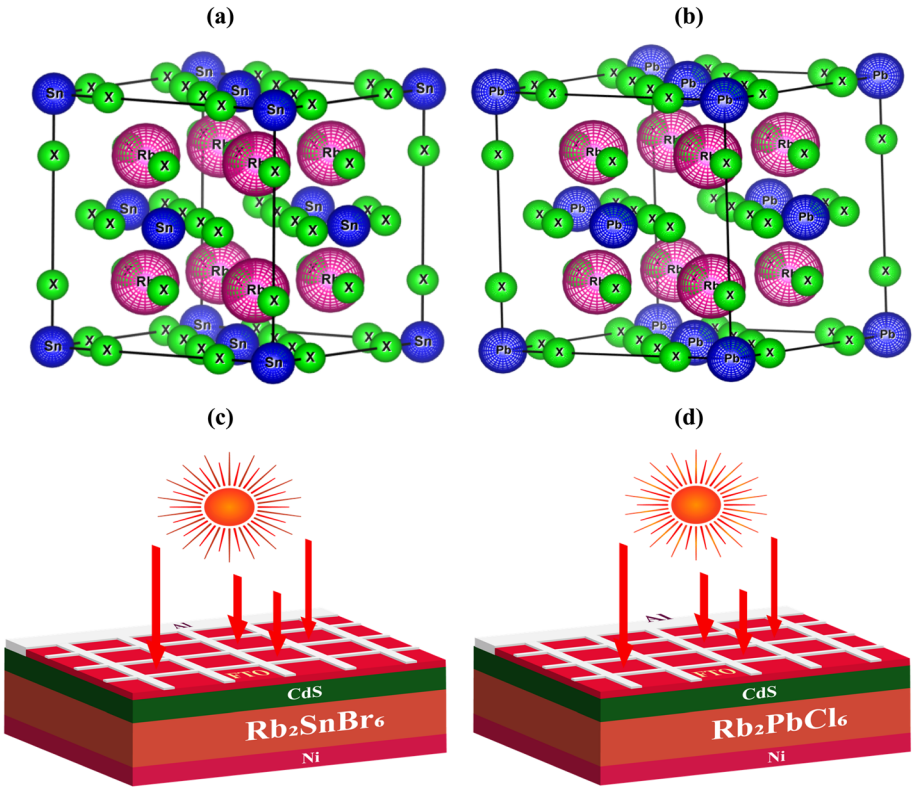

Fig. 1 Primitive crystalline unit cell of (a) Rb_2SnX_6 and (b) Rb_2PbX_6 and schematic design of the solar cell architectures for (c) Rb_2SnBr_6 and (d) Rb_2PbCl_6 double perovskite compounds.

Table 1 The bandgap, unit cell volume & formation enthalpy of the compounds Rb_2BX_6 (B = Sn/Pb, X = Cl/Br) by varying different functions

References	Compounds	Band gap, eV	Lattice constants (Å)	Density, g cm^{-3}	Unit cell volume, V (Å^3)	Formation enthalpy, ΔH_f (eV per atom)	Function/ method
This work	Rb_2SnCl_6	2.646	7.581	2.707	308.174	−3.411	GGA-PBE
	Rb_2SnBr_6	1.451	7.933	3.617	353.036	−3.019	
	Rb_2PbCl_6	1.379	7.697	3.042	322.443	−3.301	
	Rb_2PbBr_6	0.357	8.130	4.019	354.245	−2.935	
	Rb_2SnCl_6	4.231	7.581	2.727	308.145	—	Hybride-HSE06
	Rb_2SnBr_6	2.828	7.932	3.724	352.497	—	
	Rb_2PbCl_6	1.946	7.697	3.134	322.462	—	
	Rb_2PbBr_6	1.742	8.129	4.136	354.285	—	
	Rb_2SnCl_6	2.572	7.320	—	275.548	—	GGA-PBESOL
	Rb_2SnBr_6	1.178	7.605	—	308.369	—	
	Rb_2PbCl_6	1.396	7.697	—	293.009	—	
	Rb_2PbBr_6	0.277	7.437	—	326.250	—	
	Rb_2SnCl_6	2.982	7.581	—	274.806	—	*m*-GGA
	Rb_2SnBr_6	1.961	7.932	—	351.806	—	
	Rb_2PbCl_6	1.631	7.697	—	291.031	—	
	Rb_2PbBr_6	0.946	7.678	—	381.810	—	
49	Na_2SnCl_6	2.77	10.67	—	—	−3.203	GGA-PBE
	Na_2SnBr_6	1.12	10.88	—	—	−3.119	
	Na_2SnCl_6	3.98	—	—	—	—	Hybride-HSE06
	Na_2SnBr_6	3.28	—	—	—	—	
50	K_2SnCl_6	4.54	9.10	—	—	—	Experimental
	K_2SnBr_6	3.27	10.48	—	—	—	
	K_2SnI_6	1.90	—	—	—	—	
48	Rb_2SnBr_6	1.28	—	—	333.270	—	Theoretical
47	Rb_2SnBr_6	4.790	10.123	3.22	—	—	Experimental
51	Cs_2SnCl_6	3.90	—	—	—	—	Theoretical
	Cs_2SnBr_6	2.70	—	—	—	—	
	Cs_2SnI_6	1.26	—	—	—	—	

reported as 7.932 Å using the HSE06 hybrid functional, which is almost identical to our value, while a slightly larger lattice constant of 10.123 Å was observed experimentally.[47] Similarly, the theoretical lattice volume for Rb_2SnBr_6 was associated with a lattice constant consistent with our findings.[48] For comparison, other related halide perovskites such as Na_2SnCl_6 and Na_2SnBr_6 exhibit significantly larger lattice constants of 10.67 Å and 10.88 Å, respectively.[49] Likewise, K_2SnCl_6, K_2SnBr_6, and K_2SnI_6 display lattice constants of 9.99 Å, 10.48 Å, and 1.90 Å, respectively.[50] Furthermore, theoretical studies reported lattice constants of Cs_2SnCl_6, Cs_2SnBr_6, and Cs_2SnI_6 as 3.90 Å, 2.70 Å, and 1.26 Å, respectively.[51] Overall, our calculated lattice parameters for Rb-based compounds are consistent with previous works, while small variations arise due to different computational methods and experimental conditions. The thermodynamic stability of Rb_2BX_6 (B = Sn, Pb; X = Cl, Br) double perovskites was evaluated using formation enthalpy (ΔH_f) calculations. Using the relation eqn (2),[52]

$$\Delta H_f = E_{total}(Rb_2BX_6) - (2E_{Rb} + E_B + 6E_x) \quad (2)$$

All four compounds were found to be stable with negative formation energies. Specifically, Rb_2SnCl_6 exhibits ΔH_f = −3.41123 eV per atom, Rb_2SnBr_6 ΔH_f = −3.01976 eV per atom, Rb_2PbCl_6 ΔH_f = −3.30123 eV per atom, and Rb_2PbBr_6 ΔH_f = −2.93514 eV per atom. These results indicate that all compounds are thermodynamically favorable,[53] with Cl-based perovskites slightly more stable than their Br analogues and Pb-based compounds showing comparable stability to Sn-based ones Table 1. This stability suggests that these Rb_2BX_6 materials are promising candidates for further exploration in lead-free photovoltaic applications.

From the present calculations, the obtained unit cell volumes for Rb_2SnCl_6, Rb_2SnBr_6, Rb_2PbCl_6, and Rb_2PbBr_6 are 308.174 Å^3, 353.036 Å^3, 322.443 Å^3, and 354.245 Å^3, respectively, with corresponding densities of 2.707 g cm^{-3}, 3.617 g cm^{-3}, 3.042 g cm^{-3}, and 4.019 g cm^{-3}. The substitution of Cl with the larger Br anion increases the cell volume, as observed in both Sn- and Pb-based compounds (Rb_2SnCl_6 → Rb_2SnBr_6 and Rb_2PbCl_6 → Rb_2PbBr_6) Table 2. Conversely, the density shows a systematic increase with the incorporation of the heavier Br atom, reflecting the strong dependence of density on atomic mass. Furthermore, comparing Sn- and Pb-based systems reveals that Pb substitution results in slightly larger volumes

Table 2 Tolerance factor variation in Rb_2BX_6 double perovskites

Materials	r_{Rb}	r_B	r_X	Tolerance factor (t)
Rb_2SnCl_6	1.61	0.69	1.81	0.9672
Rb_2SnBr_6	1.61	0.69	1.96	0.9526
Rb_2PbCl_6	1.61	1.19	1.81	0.8060
Rb_2PbBr_6	1.61	1.19	1.96	0.8014

and higher densities than their Sn counterparts, consistent with the heavier atomic weight of Pb. These observations confirm that both the type of halogen (Cl *vs.* Br) and the choice of B-site cation (Sn *vs.* Pb) significantly influence the structural compactness and mass density of the perovskites.[47–51] The tolerance factor (t) is crucial in perovskite research because it helps predict the structural stability and symmetry of the crystal. The relation of eqn (3) has computed the tolerance factor (t).[54]

$$t = \frac{(r_{Rb} + r_X)}{\sqrt{2}(r_B + r_X)} \quad (3)$$

where r_{Rb}, r_B, and r_X are the atomic radii of Rb, Sn/Pb, and Cl/Br, respectively. Perovskite structures are generally stable when t lies between 0.8 and 1.0,[55] with values between 0.9 and 1.0 indicating more stable and well-ordered structures.[56]

For Rb_2BX_6 perovskites, the tolerance factor ranges from 0.8014 to 0.9672, indicating that all the studied materials are structurally stable. Among them, Rb_2SnCl_6 shows the highest t value (0.9672), representing the most well-balanced and stable structure, while Rb_2SnBr_6 (0.9526) exhibits a slight decrease due to the larger Br^- ion. Rb_2PbCl_6 (0.806) and Rb_2PbBr_6 (0.8014) have lower tolerance factors, suggesting minor lattice distortions caused by the larger Pb^{2+} ion. Overall, while all compounds are stable, the B-site cation and halide size influence subtle variations in structural stability and lattice ordering, consistent with trends observed in rubidium-based perovskites.

3.2 Mechanical properties

Elastic constants play a crucial role in determining mechanical properties like stiffness, machinability, hardness, ductility, and stability.[57] The mechanical properties of Rb_2BX_6 materials, including the Kleinman parameter (ζ), Cauchy pressure (C_p), Anisotropic shear constant (C_s), bulk modulus (B), shear modulus (G), Young's modulus (Y), Poisson's ratio (ν), and Pugh's ratio (B/G), are presented in Table 3. All elastic constants (C_{11}, C_{12}, and C_{44}) are positive, confirming that these materials meet the Born stability criteria (see eqn (4)),[58] as shown in Table 3. Thus, Rb_2SnCl_6, Rb_2SnBr_6, Rb_2PbCl_6, and Rb_2PbBr_6 are mechanically stable.

$$C_{11} > 0,\ 4C_{44} > 0, C_{11} - C_{12} > 0 \text{ and } C_{11} + 2C_{12} > 0 \quad (4)$$

Table 3 presents a detailed analysis of the Kleinman parameter (ζ) (see eqn (5)), which indicates the relative preference of a material for bond bending over bond stretching, thereby influencing its mechanical flexibility.[59]

$$\zeta = \frac{C_{11} + 8C_{12}}{7C_{11} + 2C_{12}} \quad (5)$$

Among the studied compounds, Rb_2PbBr_6 exhibits the highest ζ value (0.885); however, the toxicity associated with lead limits its practical relevance. Notably, Rb_2SnBr_6 shows the second-highest ζ value (0.821), making it a more favorable candidate. The greater bond-bending adaptability of Rb_2SnBr_6 suggests enhanced mechanical resilience, which is advantageous for potential optoelectronic and photovoltaic applications.

The Cauchy pressure (C_P) is a key parameter for assessing mechanical stability (see eqn (6)),[60] distinguishing between ductile and brittle behavior.[61]

$$Cp = C_{12} - C_{44} \quad (6)$$

A positive C_P indicates ductility (greater plastic deformation), while a negative C_P suggests brittleness (higher fracture tendency).[62] The C_P values for Rb_2BX_6 materials reveal distinct mechanical characteristics. Rb_2SnCl_6 (−0.032 GPa) and Rb_2PbCl_6 (−2.196 GPa) exhibit negative C_P, indicating a brittle nature due to strong covalent bonding. In contrast, Rb_2SnBr_6 (15.818 GPa) shows high ductility, making it suitable for flexible optoelectronic applications. Rb_2PbBr_6 (0.166 GPa), with a slightly positive C_P, falls between brittle and ductile, offering moderate mechanical adaptability. The bulk modulus (B) quantifies a material's resistance to uniform compression (see eqn (7)).[60]

$$B = \frac{B_V + B_R}{2} \quad (7)$$

Rb_2SnBr_6 exhibits the highest B (26.603 GPa), making it the least compressible, while Rb_2PbBr_6 (4.828 GPa) is the most

Table 3 Mechanical properties of Rb_2BX_6 double perovskites

	This work			
Mechanical values	Rb_2SnCl_6	Rb_2SnBr_6	Rb_2PbCl_6	Rb_2PbBr_6
C_{11} (GPa)	12.999	32.004	10.901	5.425
C_{12} (GPa)	3.841	23.902	3.843	4.530
C_{44} (GPa)	3.873	8.084	6.039	4.364
Kleinman parameter, ζ	0.443	0.821	0.704	0.885
Cauchy pressure, C_P	−0.032	15.818	−2.196	0.166
Bulk modulus (B)	6.894	26.603	6.196	4.828
Shear modulus (G)	4.141	6.126	4.868	1.883
Young's modulus (Y)	10.351	17.069	11.574	5.001
Poisson's ratio (ν)	0.249	0.393	0.188	0.327
Pugh's modulus ratio (B/G)	1.664	4.342	1.272	2.563
Machinability index, μ_M	1.780	3.290	1.025	1.106

compressible. The shear modulus (G) measures resistance to shape deformation under shear stress (see eqn (8)),[60] with Rb_2SnBr_6 (6.126 GPa) showing the highest value, indicating superior structural rigidity.

$$G = \frac{G_V + B_R}{2} \tag{8}$$

Similarly, Young's modulus (Y) quantifies stiffness in tension, where a higher Y signifies greater rigidity (see eqn (9)).[60]

$$Y = \frac{9BG}{(3B + G)} \tag{9}$$

Rb_2SnBr_6, with the highest Y (17.069 GPa), confirms its superior mechanical strength compared to the other perovskites. The Poisson's ratio (ν) and Pugh's ratio (B/G) distinguish ductility variations (see eqn (10)).[63]

$$\nu = \frac{3B - 2G}{2(3B + G)} \tag{10}$$

Materials are classified as brittle (B/G < 1.75, ν < 0.26) or ductile (B/G > 1.75, ν > 0.26).[64] A higher ν indicates greater ductility, as seen in Rb_2SnBr_6 (ν = 0.393), while lower values, like in Rb_2PbCl_6 (ν = 0.188), suggest brittleness. Similarly, Pugh's ratio reflects mechanical behavior; Rb_2PbBr_6 (B/G = 2.563) is the most ductile, whereas Rb_2SnBr_6 (B/G = 0.708) is the most brittle. Thus, Rb_2SnBr_6 exhibits superior ductility and mechanical stability. The machinability index (μ_m), defined in eqn (11), indicates the ease of processing of a material. Higher μ_m values correspond to better machinability, reflecting lower resistance to cutting, shaping, or fabrication.[65]

$$\mu_M = \frac{B}{C_{44}} \tag{11}$$

Among the Rb_2BX_6 compounds, Rb_2SnBr_6 has the highest μ_m (3.290), indicating good ductility, while Rb_2SnCl_6 is moderately machinable (1.780). The Pb-based compounds, Rb_2PbCl_6 (1.025) and Rb_2PbBr_6 (1.106), are less machinable due to brittleness. Overall, Sn-based Rb_2BX_6 compounds are easier to process than Pb-based analogs, showing that B-site substitution strongly affects mechanical workability.

3.3 Electronic properties

A comprehensive understanding of the electronic properties of Rb-based perovskite materials necessitates an in-depth analysis of their electronic band structure and density of states (DOS).[66] These evaluations not only classify materials as semiconducting, insulating, or metallic but also provide insights into their bonding characteristics and energy band gaps.[58,67] The electronic band structure is obtained *via* density functional theory (DFT) calculations, following structural optimization and k-point sampling within the first Brillouin zone.

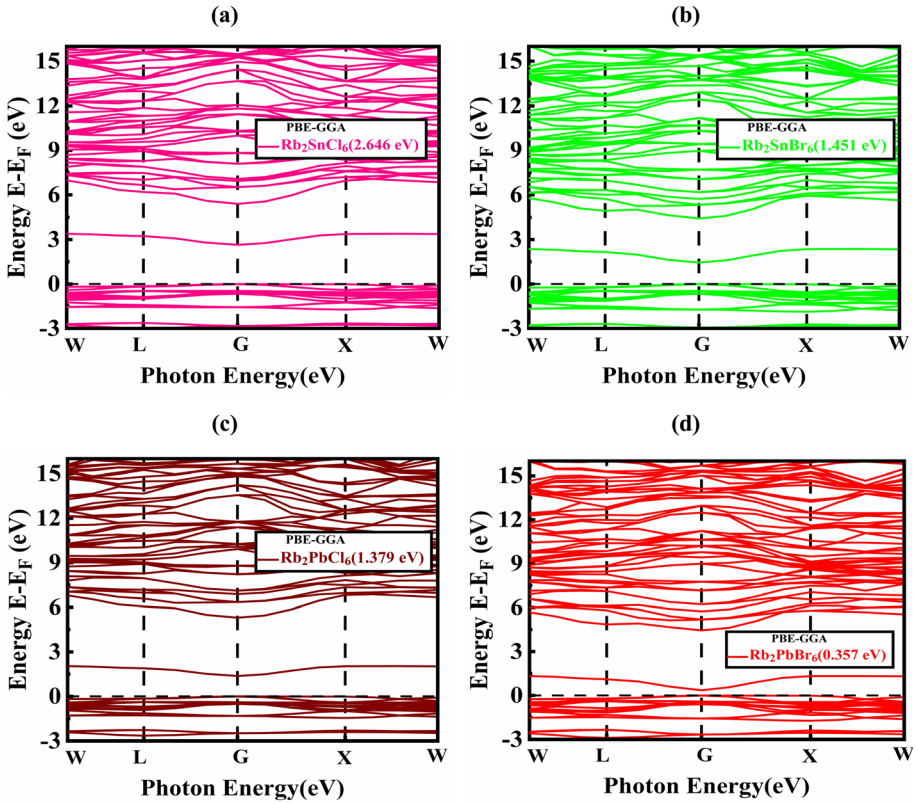

Fig. 2 Energy band gap values of (a) Rb_2SnCl_6, (b) Rb_2SnBr_6, (c) Rb_2PbCl_6, and (d) Rb_2PbBr_6 compounds calculated using the PBE-GGA exchange–correlation functional.

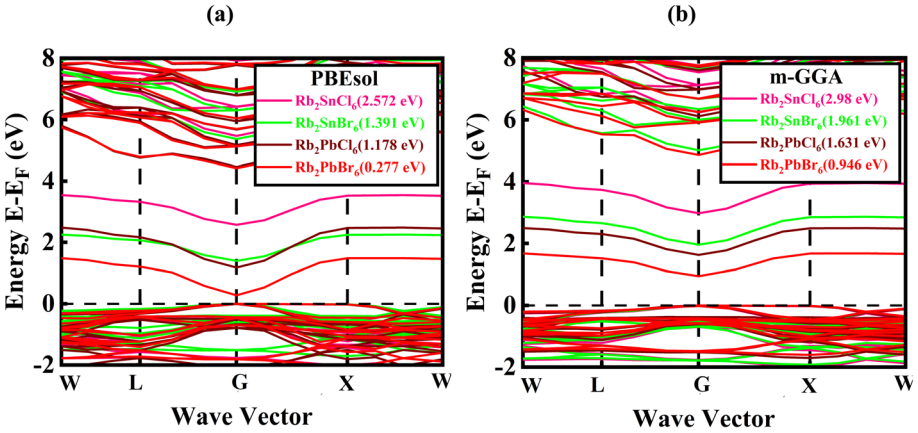

Fig. 3 Energy band gap values of Rb_2BX_6 compounds using (a) GGA-PBEsol and (b) *m*-GGA exchange–correlation functional.

The electronic band gaps of Rb_2SnCl_6, Rb_2SnBr_6, Rb_2PbCl_6, and Rb_2PbBr_6 were calculated using four exchange–correlation functionals: GGA-PBE, GGA-PBEsol, *m*-GGA, and hybrid HSE06. Using GGA-PBE, the band gaps are 2.646, 1.451, 1.379, and 0.357 eV, respectively (Fig. 2a–d). The GGA-PBEsol functional yields slightly smaller gaps (2.572, 1.391, 1.178, and 0.277 eV, Fig. 3a), reflecting its systematic tendency to slightly compress lattice parameters, which reduces the band gap. *m*-GGA (*meta*-GGA) predicts intermediate values (2.980, 1.961, 1.631, and 0.946 eV, Fig. 3b), capturing enhanced gradient corrections that moderately increase the gap compared to PBEsol.

The HSE06 hybrid functional, which incorporates a fraction of exact exchange, significantly increases the band gaps to 4.231, 2.828, 1.946, and 1.742 eV, respectively (Fig. 4a–d), providing the most accurate estimate consistent with experimental trends in similar perovskites. A comparison with earlier reports shows good agreement. For instance, Na_2SnCl_6 (2.77 eV) and Na_2SnBr_6 (1.12 eV) using GGA-PBE follow the same halogen-dependent narrowing trend as in our Rb-based systems.[49] Similarly, experimental values for K_2SnCl_6 (4.54 eV), K_2SnBr_6 (3.27 eV), and K_2SnI_6 (1.90 eV) also confirm the systematic reduction of the band gap with increasing halogen

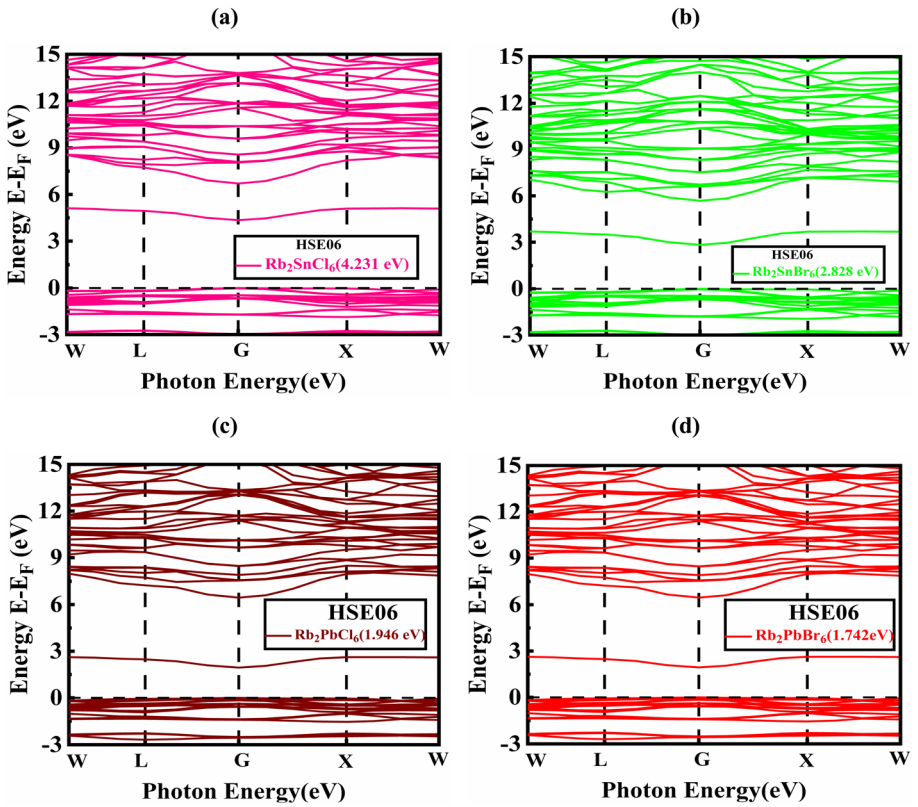

Fig. 4 Energy band gap values of (a) Rb_2SnCl_6, (b) Rb_2SnBr_6, (c) Rb_2PbCl_6, and (d) Rb_2PbBr_6 compounds calculated using the hybrid HSE06 exchange–correlation functional.

size.[50] Theoretical calculations reported Cs_2SnCl_6 (3.90 eV), Cs_2SnBr_6 (2.70 eV), and Cs_2SnI_6 (1.26 eV),[51] again consistent with our observations. Additionally, reported theoretical and experimental results for Rb_2SnBr_6 show band gaps of 1.28 eV and 4.79 eV,[47,48] which align closely with our PBE and HSE06 values, respectively.

The variation in band gaps across the compounds arises from both cation and halide effects. Substituting Sn with Pb reduces the gap due to the larger spin–orbit coupling and more diffuse Pb 6s/6p orbitals, which lower the conduction–valence band separation.

Similarly, replacing Cl with Br decreases the gap, as Br 4p orbitals are higher in energy than Cl 3p orbitals, elevating the valence band maximum. Consequently, Rb_2SnCl_6 exhibits the widest gap, while Rb_2PbBr_6 has the smallest, a trend consistent across all functionals. The choice of functional influences the absolute values but preserves the relative trends: PBE tends to slightly underestimate gaps due to self-interaction errors, PBEsol reduces gaps further due to lattice compression, *m*-GGA improves description with gradient corrections, and HSE06 provides the most reliable quantitative values. These observations highlight the importance of using multiple functionals to balance computational efficiency and predictive accuracy in perovskite band structure calculations.

Furthermore, the analysis of the PDOS and TDOS diagrams in Fig. 5a–d corroborates the band gap values obtained from the band structure calculations using the GGA-PBE functional, which provides a computationally efficient and reliable estimate. Notably, these calculations require relatively short computational time, making them suitable for rapid screening of multiple compounds. The PDOS graphs in Fig. 5 highlight the distinct electronic properties of Rb_2SnCl_6, Rb_2SnBr_6, Rb_2PbCl_6, and Rb_2PbBr_6.

In Rb_2SnCl_6 (Fig. 5a), the valence band is primarily composed of Cl-3p states with contributions from Sn-5s, while the conduction band mainly consists of Sn-5p and Rb-4p states, indicating a wide band gap and semiconducting behavior. Similarly, Rb_2SnBr_6 in Fig. 5b follows this trend, but the presence of Br-4p states shifts the conduction band downward, reducing the band gap and enhancing visible-light absorption. In Rb_2PbCl_6 Fig. 5c, the valence band originates from Cl-3p and Pb-6s states, while the conduction band is primarily composed of Pb-6p states, resulting in a moderate band gap. Among the four materials, Rb_2PbBr_6 Fig. 5d exhibits the smallest band gap, with Br-4p and Pb-6s states dominating the valence band, while Pb-6p states form the conduction band, enhancing its optical absorption properties.

3.4 Optical properties

Optical properties describe how a material interacts with light—through absorption, reflection, transmission, or refraction of electromagnetic radiation across different energy ranges.[65,68,69] Key parameters such as the real and imaginary parts of the dielectric function, optical conductivity, absorption coefficient,

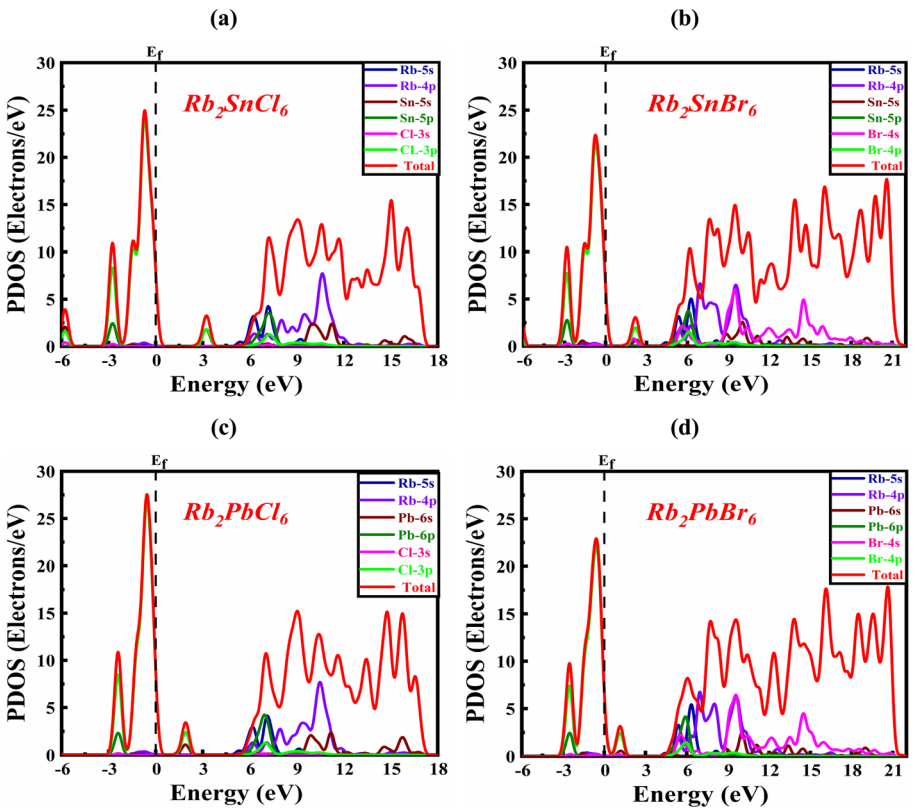

Fig. 5 The Partial Density of States (PDOS) of (a) Rb_2SnCl_6, (b) Rb_2SnBr_6, (c) Rb_2PbCl_6, and (d) Rb_2PbBr_6 double perovskite materials using the PBE-GGA exchange–correlation functional.

refractive index, reflectivity, and energy loss function reveal how efficiently a material can capture and utilize photons. In solar cells, these properties are crucial as they govern light absorption, exciton generation, and overall photovoltaic efficiency. Using first-principles Density Functional Theory (DFT) in CASTEP within Materials Studio, the intrinsic optical response can be predicted, while SCAPS-1D simulations incorporate this data—such as bandgap, absorption coefficient, and dielectric constants—to evaluate and optimize device performance under realistic conditions. Such understanding aids in selecting suitable absorber layers, engineering band alignments, and improving device architecture, thereby guiding the design of efficient and stable solar cells.

The dielectric function, $\varepsilon(\omega)$, is a complex optical parameter that describes how a material interacts with electromagnetic radiation across different photon energies. It consists of the real part, $\varepsilon_r(\omega)$, which indicates how light is slowed down and polarized within the material, and the imaginary part, $\varepsilon_{imag}(\omega)$, which represents the amount of energy absorbed from the electromagnetic wave.[70]

$$\varepsilon(\omega) = \varepsilon_r(\omega) + i\varepsilon_{imag}(\omega) \quad (12)$$

In the context of solar cells and optoelectronic applications, $\varepsilon(\omega)$ is critically important because it reveals the material's ability to store and absorb light energy, providing insights into its electronic transitions, optical losses, and overall light–matter interaction.[23] A high $\varepsilon_{imag}(\omega)$ in the visible region, for example, signifies strong photon absorption, which is essential for efficient charge generation, while $\varepsilon_r(\omega)$ helps optimize light propagation and minimize reflection losses. Thus, calculating and analyzing the dielectric function through DFT-based tools like CASTEP supports the design and optimization of high-performance photovoltaic and

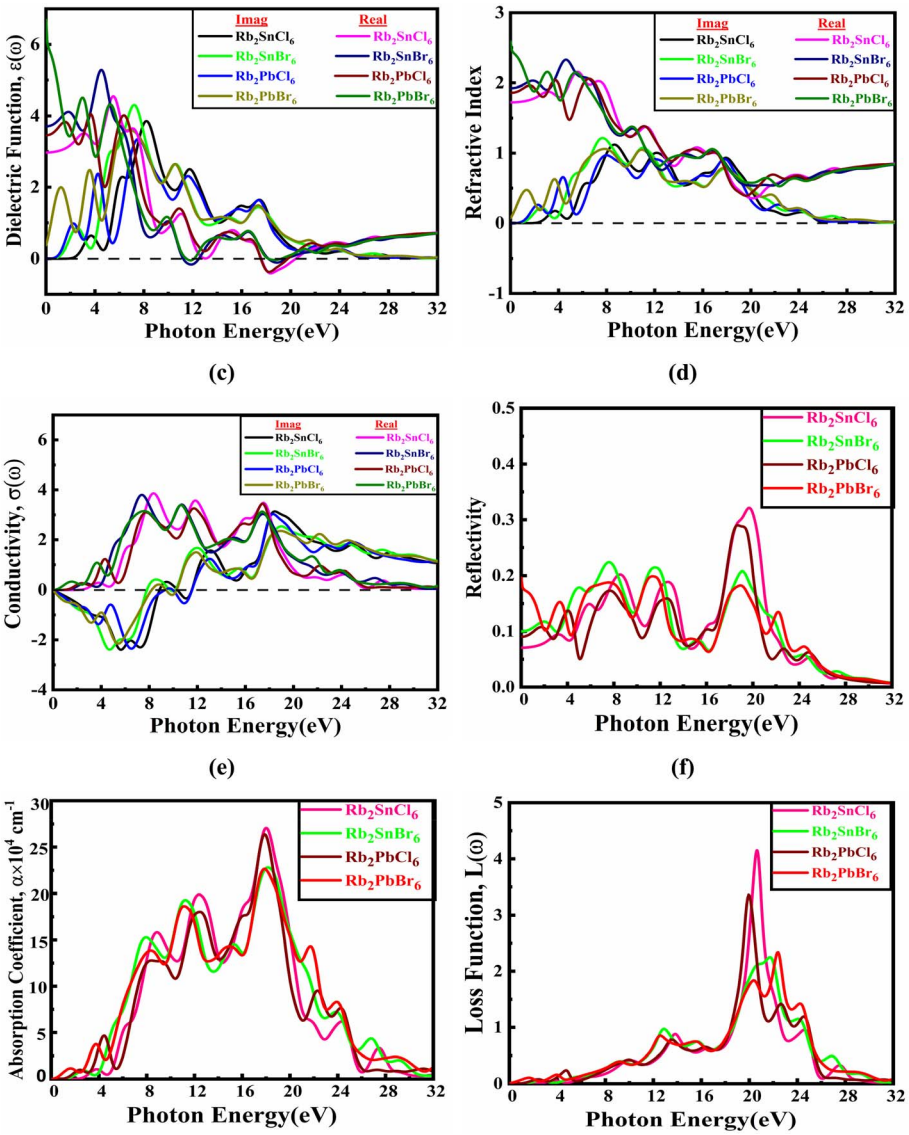

Fig. 6 Presents Rb_2BX_6 (B = Sn/Pb, X = Cl/Br) (a) dielectric function, (b) refractive index, (c) conductivity, (d) reflectivity, (e) absorption coefficient, and (f) electron loss function.

optoelectronic devices. eqn (13) and (14) are the expressions for the dielectric function.[71,72]

$$\varepsilon_r(\omega) = 1 + \frac{2}{\pi} P \int_0^{\infty} \frac{\omega' \varepsilon_2\left(\omega'\right)}{\omega'^2 - \omega^2} \mathrm{d}\omega' \tag{13}$$

$$\varepsilon_{imag}(\omega) = \frac{2\pi e^2}{\Omega \varepsilon_0} \sum_{k,v,c} |\langle \Psi_k{}^c | \hat{u} \cdot \vec{r} | \Psi_k{}^v \rangle|^2 \delta(E_k{}^c - E_k{}^v - E) \tag{14}$$

The calculated static dielectric constant values, $\varepsilon_r(0)$, for cubic Rb_2SnCl_6, Rb_2SnBr_6, Rb_2PbCl_6, and Rb_2PbBr_6 double perovskites were 3.40, 3.95, 4.05, and 6.01, respectively. Among these, Rb_2PbBr_6 exhibits the highest $\varepsilon_r(0)$ value. With increasing photon energy, distinct peaks are observed in the frequency-dependent dielectric function ($\varepsilon_r(\omega)$), after which the real part of the dielectric function gradually decreases and approaches zero beyond 12 eV for all compounds. Although Rb_2PbBr_6 shows the strongest dielectric screening, its low band gap and the toxicity of lead make it less suitable for practical applications. In contrast, Rb_2SnBr_6 offers a more balanced dielectric response with moderate $\varepsilon_r(\omega)$ while avoiding lead-related toxicity, making it a more favorable candidate for optoelectronic applications. The static dielectric function is an important parameter for solar cell materials, as it directly influences charge separation, exciton dissociation, and overall photovoltaic performance. The imaginary part of the dielectric function, $\varepsilon_{imag}(\omega)$, plays a key role in understanding the electronic band gap. This band gap is closely linked to the energy of interband transitions near the Fermi level and significantly affects the optical absorption properties of the material.[73,74] The $\varepsilon_{imag}(\omega)$ values of Rb_2BX_6 show a wide absorption range in their spectra. As illustrated in Fig. 6a, the main peaks of $\varepsilon_{imag}(\omega)$ are located at 0 eV, 1.379 eV, 1.451 eV, and 2.646 eV for the double perovskites Rb_2PbBr_6, Rb_2PbCl_6, Rb_2SnBr_6, and Rb_2SnCl_6, respectively. Optical properties of a compound can ascertain how electronic transitions can respond to changing perturbations in ground state, as discussed in ref. 75. In optical properties, initially the complex dielectric constant is examined from which all other parameters are evaluated.

Beyond these points, the refractive index $\eta(\omega)$ for both compounds decline as ω rises. The refractive index $\eta(\omega)$ consists of real η_1 and imaginary η_2 parts, which are represented as.[76] The figure Fig. 6b, presents the refractive index $\eta(\omega)$ (both real η_1 and imaginary η_2 components) as a function of photon energy for Rb_2BX_6 (B = Sn, Pb; X = Cl, Br) compounds, where Rb_2SnBr_6 and Rb_2PbCl_6 exhibit prominent optical responses. Rb_2SnBr_6 starts at ~2.3 at 0 eV, with peaks at 1.8 (~5 eV) and 1.5 (~10 eV), while Rb_2PbCl_6 begins at ~2.1, peaking at 1.7 (~6 eV) and 1.3 (~10 eV); their imaginary parts show strong absorption around 4–10 eV. All compounds tend to converge to zero beyond 20 eV, highlighting Rb_2SnBr_6 and Rb_2PbCl_6 as highest promising for optoelectronic applications. The Fig. 6c illustrates the optical conductivity $\sigma(\omega)$ of Rb_2BX_6 (B = Sn, Pb; X = Cl, Br) as a function of photon energy. Rb_2SnBr_6 and Rb_2PbCl_6 show strong optical responses, with real conductivity peaking around 4.5 at ~8 eV for Rb_2SnBr_6 and 4.2 at ~10 eV for Rb_2PbCl_6, indicating efficient photon absorption. All compounds exhibit fluctuations, with conductivity declining beyond 20 eV, suggesting diminishing optical transitions at higher energies. The Fig. 6d depicts the reflectivity $R(\omega)$ of Rb_2BX_6 (B = Sn, Pb; X = Cl, Br) as a function of photon energy, eV. Rb_2SnBr_6 and Rb_2PbCl_6 show moderate reflectivity, peaking around 0.22 at ~10 eV for Rb_2SnBr_6 and 0.3 at ~20 eV for Rb_2PbCl_6, indicating their optical response. All compounds exhibit fluctuations, with reflectivity generally remaining below 0.5, suggesting strong light absorption in the studied energy range. The optical absorption coefficient indicates how effectively a material absorbs light, which is vital for solar cells, especially within the 1.5–4.0 eV range.[77,78] Extending the analysis up to 30 eV (ref. 79–81) also reveals deeper electronic transitions, relevant for UV photodetectors, PL behavior, and radiation shielding applications.[82,83] Fig. 6e first highlights the visible absorption range (1.5–4.0 eV), confirming that Rb_2BX_6 materials exhibit strong absorption in the visible spectrum. Additionally, the absorption spectra of Rb_2SnBr_6 and Rb_2PbCl_6 show distinct peaks: Rb_2SnBr_6 peaks at ~8, 13, and 18 eV with intensities up to 25×10^4 cm^{-1}, while Rb_2PbCl_6 peaks at ~7, 12, 16, and 20 eV, exceeding 27×10^4 cm^{-1} near 17–20 eV. These high-energy peaks indicate strong ultraviolet absorption, making them suitable for UV detection, PL, and related optoelectronic applications. The sharper features in Rb_2PbCl_6 suggest stronger absorption transitions, whereas Rb_2SnBr_6 shows a smoother absorption profile. Finally, the loss function $L(\omega)$ in Fig. 6f for Rb_2SnBr_6 and Rb_2PbCl_6 shows prominent peaks in the 18–24 eV range, with Rb_2PbCl_6 peaking around 21 eV and Rb_2SnBr_6 slightly lower. Rb_2SnCl_6 exhibits the highest peak (~4.5) at ~21 eV, indicating strong plasmonic resonance, while Rb_2PbBr_6 and Rb_2PbCl_6 display similar peak positions with varying intensities. All compounds show minimal loss below 15 eV, with a sharp increase beyond 18 eV, highlighting the role of Sn *vs.* Pb and Cl *vs.* Br in plasmonic excitations and energy dissipation.

3.5 Anisotropy properties

For an isotropic material, $A = A_1 = A_2 = A_3 = 1$, and the variation from unity corresponds to the anisotropy of a material.[84,85]

$$A^U = \frac{B_V}{B_r} + 5\frac{G_V}{B_R} - 6 \geq 0 \tag{15}$$

$$A^B = \frac{B_V - B_R}{B_V + B_R} \tag{16}$$

$$A^{eq} = \left(1 + \frac{5}{12}A^U\right) + \sqrt{\left(1 + \frac{5}{12}A^U\right)^2 - 1} \tag{17}$$

$$A_G = \frac{G_V - G_R}{G_V + G_R} \tag{18}$$

Finally, the anisotropy factors (A, A^U, A_{eq}, A_G) assess how elastic properties vary in different crystallographic directions. The Zener anisotropic factor (A) is particularly significant, where $A = 1$ denotes a perfectly isotropic material. Larger deviations from 1 indicate anisotropy, meaning the material's properties depend heavily on direction.

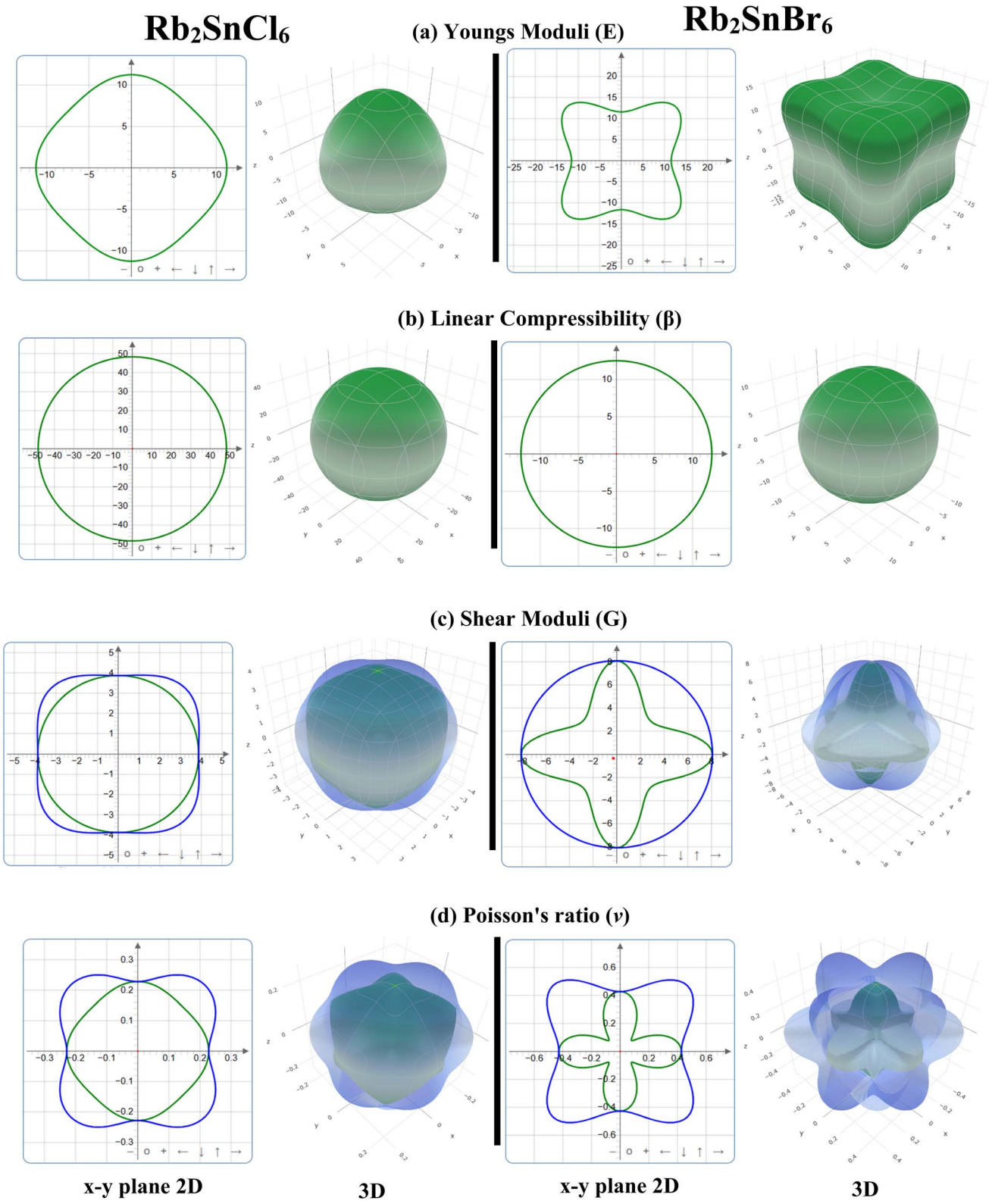

Fig. 7 Anisotropic 2D and 3D Spatial dependence representation of (a) Youngs moduli, (b) linear compressibility, (c) shear moduli, (d) Poisson's ratio of the Rb_2BX_6 materials.

Rb_2PbBr_6, with an extremely high A value of 9.751, is highly anisotropic, meaning its mechanical behavior changes significantly depending on the direction of applied force. In contrast, Rb_2SnCl_6, with an A value of 0.845, is the most isotropic, meaning it behaves uniformly in all directions. The provided Fig. 7 and 8 represent a comprehensive visualization of the

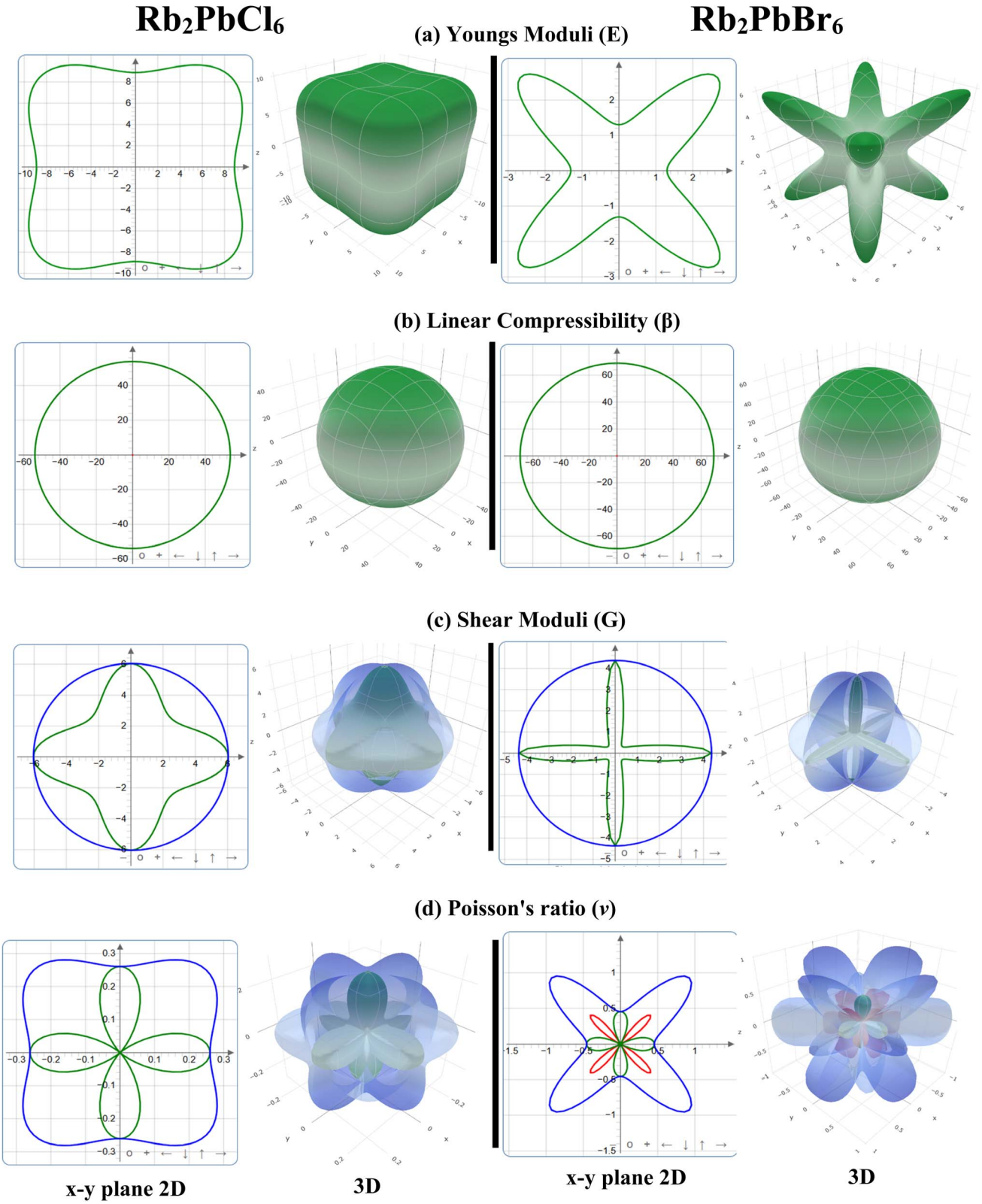

Fig. 8 Anisotropic 2D and 3D Spatial dependence representation of (a) Youngs moduli, (b) linear compressibility, (c) shear moduli, (d) Poisson's ratio of the Rb_2BX_6 materials.

elastic anisotropy of different halide perovskite compounds, likely Rb_2SnCl_6, Rb_2SnBr_6, Rb_2PbCl_6, and Rb_2PbBr_6. The figures include 2D polar plots and corresponding 3D surfaces, illustrating how elastic properties vary with crystallographic direction. Fig. 7 and 8 illustrate the Anisotropy index for Rb_2BX_6 materials, representing each row as depicting a different

mechanical parameter, such as Young's modulus, shear modulus, or Poisson's ratio. The leftmost column contains 2D polar plots, showing the directional dependence of a given property, while the adjacent 3D plots provide a spatial representation of the same data. The rightmost columns contain additional 2D and 3D visualizations, often incorporating multiple data sets (denoted by green and blue curves), possibly comparing theoretical and experimental values or different anisotropy measures. The diversity in shape and symmetry among the figures reflects the varying degrees of anisotropy in these materials. More spherical shapes, as seen in the middle row, suggest nearly isotropic behavior, indicating uniform mechanical responses in all directions. In contrast, highly distorted or lobed shapes, particularly in the top and bottom rows, reveal strong anisotropic behavior, meaning the material exhibits direction-dependent stiffness or flexibility.[42,43] This anisotropy is critical in determining mechanical performance for applications in flexible electronics, optoelectronics, and thermoelectric materials. The contrasting line colors and the interplay of smooth *versus* wavy contours likely indicate different computational models or comparative analyses of elastic responses.[86]

3.6 Phonon analysis

Phonon analysis studies the quantized vibrations of atoms in a crystal lattice, providing insight into the dynamic behavior of materials.[87] Calculating phonon dispersion curves allows the assessment of dynamical stability, where entirely positive phonon frequencies indicate a stable structure, while imaginary (negative) frequencies reveal potential lattice instabilities or structural distortions.[88] Beyond stability, phonon analysis is crucial for understanding thermal properties such as heat capacity and thermal conductivity, electron–phonon interactions affecting electrical and superconducting behavior, and optical characteristics like infrared absorption and Raman activity.[79]

Therefore, phonon calculations are essential for predicting material performance, guiding chemical substitutions, and designing compounds with robust structural, thermal, and optoelectronic properties. Fig. 9 illustrates the phonon dispersion curves of the cubic double perovskites along the high-symmetry directions *W–L–Γ–X–W–R*, with (a) Rb_2SnCl_6, (b) Rb_2SnBr_6, (c) Rb_2PbCl_6, and (d) Rb_2PbBr_6. Phonon dispersion analysis is a critical tool for assessing the dynamical stability of crystalline materials, as negative frequencies (imaginary modes) indicate potential lattice instabilities that could lead to phase transitions or structural distortions. In the present case, the Cl-based compounds, Rb_2SnCl_6 and Rb_2PbCl_6, display entirely positive phonon frequencies across the full Brillouin zone. This observation confirms the absence of any unstable vibrational modes and suggests that these materials are dynamically stable. The high-frequency optical phonon branches, primarily associated with the vibrations of the lighter Cl atoms, reflect strong bonding interactions within the lattice, contributing to the

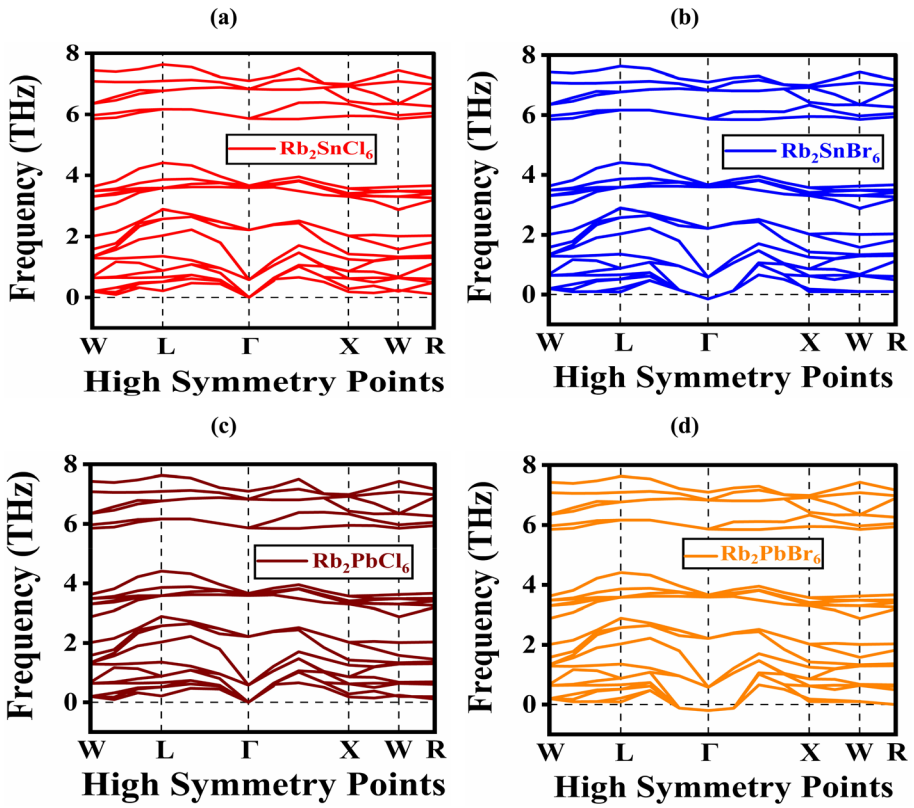

Fig. 9 Phonon dispersion curves of (a) Rb_2SnCl_6, (b) Rb_2SnBr_6, (c) Rb_2PbCl_6 and (d) Rb^2PbBr_6 cubic double perovskites along the high-symmetry directions.

rigidity and robustness of the crystal structure. Conversely, the Br-based analogues, Rb_2SnBr_6 and Rb_2PbBr_6, exhibit phonon branches that dip below zero near certain high-symmetry points, signaling the presence of imaginary frequencies. These negative modes indicate lattice instabilities, likely arising from the larger atomic radius and higher mass of Br compared to Cl, which weaken the restoring forces in the lattice. Consequently, the Br-substituted compounds are prone to structural distortions or phase transitions under ambient conditions, reflecting softer bonding characteristics and reduced lattice stiffness.

3.7 Population analysis

The charge analysis of halide perovskites (Rb_2PbCl_6, Rb_2PbBr_6, Rb_2SnCl_6, and Rb_2SnBr_6) in Table 4 provides insights into their electronic structure, bonding nature, and charge distribution. Charge spilling, Mulliken atomic populations, and Mulliken and Hirshfeld charges reveal how electrons are distributed among the atomic species (Rb, Pb/Sn, and Cl/Br), impacting their mechanical and electronic properties. Charge spilling, which quantifies electron density outside atomic spheres, varies among these compounds, with Rb_2SnCl_6 having the highest (0.20%) and Rb_2PbBr_6 the lowest (0.12%), indicating greater electron delocalization in Sn-based chlorides and more localized charge in Pb-based bromides. The Mulliken atomic populations show that Rb maintains an electron count of ~8.27 to 8.50, primarily distributed in s (~2.06 to 2.09 electrons) and p (~6.08 to 6.18 electrons) orbitals, confirming its role as an electron donor. Pb and Sn exhibit strong d-orbital occupancy (~10 electrons for Pb, lower for Sn), with Sn showing a lower total electron count (~13.05–13.52) than Pb (~21.16 to 21.39), suggesting different bonding interactions. The halide atoms (Cl and Br) primarily occupy the s (~1.88 to 1.96 electrons) and p (~5.34 to 5.45 electrons) orbitals, reinforcing their electron-accepting role.

Mulliken charge analysis confirms that Rb consistently has a positive charge (0.50 to 0.73), Pb and Sn exhibit moderate positive values (0.48 to 0.95), and halides carry negative charges (−0.25 to −0.40), highlighting the ionic nature of these materials. Among them, Sn in Rb_2SnCl_6 has the highest Mulliken charge (0.95), suggesting stronger ionic bonding compared to Pb. Hirshfeld charge analysis, which generally yields smaller charge values, similarly shows Rb with a slightly positive charge (~0.21 to 0.23), Pb and Sn with moderate positive values (~0.34 to 0.44), and halogens with negative charges (−0.14 to −0.17), reinforcing the observed charge transfer trends. Comparing Pb-based and Sn-based compounds, Sn perovskites show higher positive Sn charges and lower total electron populations, suggesting a more ionic nature, while Pb compounds exhibit stronger d-orbital contributions, indicating enhanced covalent character. Similarly, chlorides (Rb_2SnCl_6, Rb_2PbCl_6) show stronger ionic bonding due to higher halide Mulliken charges (−0.38 to −0.40) compared to bromides (−0.25 to −0.27), where charge delocalization is more prominent. These findings highlight the greater ionic nature of Rb_2SnCl_6 and the more covalent behavior of Rb_2PbBr_6, influencing their electronic structure, stability, and potential optoelectronic applications.

3.8 Optimizing solar cell simulations: a deep dive into SCAPS-1D performance

Fig. 10a and b illustrates the band structures of two HTL-free double perovskite solar cells (DPSCs), Rb_2SnBr_6 and Rb_2PbCl_6, each incorporating a different light-absorbing material. In these diagrams, E_V (eV) indicates the highest energy level of the valence band, E_C (eV) signifies the lowest energy level of the conduction band, while F_n (eV) and F_p (eV) represent the electron and hole Fermi levels, respectively. The bandgap values are 1.451 eV for Rb_2SnBr_6 and 1.376 eV for Rb_2PbCl_6. The fluorine-doped tin oxide (FTO) window layer has a wide band gap of 3.6 eV, contrasting with the n-type cadmium sulfide (CdS) electron transport layer (ETL), which features a band gap of 2.42 eV. The conduction band offset (CBO) refers to the energy gap between the conduction band minimum of the perovskite and the ETL, while the valence band offset (VBO) represents the energy difference between the valence band maximum of the perovskite and the ETL.

Table 5 presents key material parameters for the FTO, CdS, Rb_2SnBr_6, and Rb_2PbCl_6 layers used in heterostructures.

Electron affinity (χ): calculated using the equation:

Table 4 Mulliken and Hirshfeld charge analysis of different atoms of Rb_2BX_3 (B = Sn, Pb and X = Cl, Br)

Compound	Charge spilling	Species	Ion	Mulliken atomic populations					Mulliken charge	Hirshfeld charge
				s	p	d	f	Total		
Rb_2PbCl_6	0.15%	Rb	2	2.06	6.10	0.13	0.0	8.28	0.72	0.22
		Pb	1	3.60	7.56	10.0	0.0	21.16	0.84	0.44
		Cl	6	1.96	5.42	0.00	0.0	7.38	−0.38	−0.17
Rb_2PbBr_6	0.12%	Rb	2	2.09	6.16	0.25	0.0	8.50	0.50	0.21
		Pb	1	3.64	7.75	10.0	0.0	21.39	0.61	0.36
		Br	6	1.93	5.34	0.00	0.0	7.27	−0.27	−0.14
Rb_2SnCl_6	0.20%	Rb	2	2.06	6.08	0.13	0.0	8.27	0.73	0.23
		Sn	1	1.39	1.66	10.0	0.0	13.05	0.95	0.42
		Cl	6	1.96	5.45	0.00	0.0	7.40	−0.40	−0.16
Rb_2SnBr_6	0.16%	Rb	2	2.08	6.18	0.24	0.0	8.50	0.50	0.21
		Sn	1	1.67	1.85	10.0	0.0	13.52	0.48	0.34
		Br	6	1.88	5.36	0.00	0.0	7.25	−0.25	−0.14

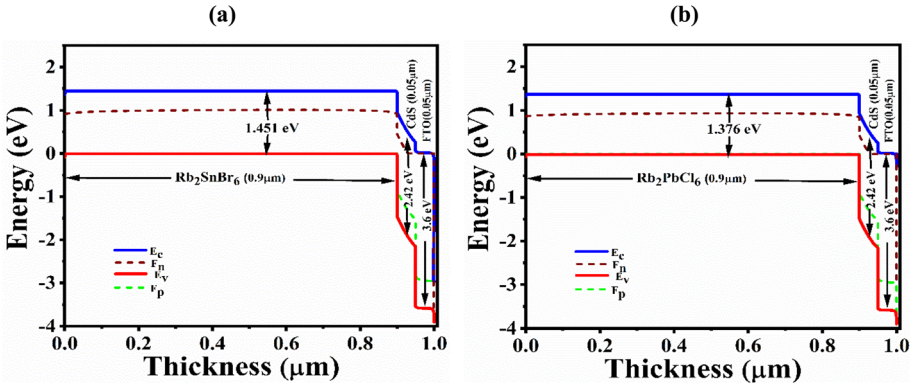

Fig. 10 Band alignment of (a) Rb_2SnBr_6 (b) Rb_2PbCl_6 structure.

Table 5 The parameters needed for configuring the simulation device architecture

Parameters	FTO[89–91]	CdS[92]	Rb_2SnBr_6	Rb_2PbCl_6
Thickness (nm)	50	50	900	900
Band gap, E_g (eV)	3.6	2.42	1.451	1.379
Dielectric permitivity, ε_r	10	9.35	3.71	3.46
Electron affinity, χ (eV)	4.5	4.30	3.860	4.910
CB effective density of states, N_C (1/cm^3)	2×10^{18}	2.2×10^{18}	9.424×10^{18}	9.633×10^{18}
VB effective density of states, N_V (1/cm^3)	1.8×10^{19}	1.8×10^{19}	1.415×10^{19}	1.741×10^{19}
Shallow uniform acceptor density, N_A (1/cm^3)	0	0	1×10^{19}	1×10^{19}
Shallow uniform donor density, N_D (1/cm^3)	1×10^{18}	1×10^{17}	0	0
Electron thermal velocity (cm s^{-1})	1×10^7	1×10^7	1×10^7	1×10^7
Hole thermal velocity (cm s^{-1})	1×10^7	1×10^7	1×10^7	1×10^7
Electron mobility, μ_n (cm^2 V^{-1} s^{-1})	50	100	100	100
Hole mobility, μ_h (cm^2 V^{-1} s^{-1})	20	25	20	50
Total defect density (cm^{-3})	1×10^{14}	1×10^{12}	1×10^{13}	1×10^{13}

$$\chi = E_{Vac} - E_{CBM} \quad (19)$$

where E_{Vac} is the vacuum level, and E_{CBM} is the conduction band minimum. This method is commonly used in first-principles studies of semiconductors.[93]

Dielectric function or relative permittivity (ε):

The frequency-dependent dielectric function

$$\varepsilon(0) = \varepsilon_r(0) + i\varepsilon_{imag}(0) \quad (20)$$

Eqn (20) represents eqn (12) evaluated at $\omega = 0$ (static limit). At zero frequency, the imaginary part becomes negligible ($\varepsilon_{imag}(0) \approx 0$), and the static dielectric constants are $\varepsilon_r(0) = 3.71$ for Rb_2SnBr_6 and $\varepsilon_r(0) = 3.46$ for Rb_2PbCl_6 and $\varepsilon_r(0)$ and $\varepsilon_{imag}(0)$ are connected through the Kramers–Kronig relations.[94]

Shallow donor and acceptor densities (N_D, N_A):

These values were adopted from literature reports on similar perovskite materials, as their direct calculation requires detailed defect energetics. The selected values are representative of solar cell device simulations.[95]

Electron and hole mobilities (μ_e, μ_h):

Mobilities were estimated using:

$$\mu = \frac{eT}{m} \quad (21)$$

where m is the effective mass (calculated from the band structure curvature) and T is the relaxation time. Since T is not explicitly calculated, we used typical values reported for similar halide perovskites.[96,97] While this approach gives approximate values, it effectively captures the trend in carrier transport.

The standard formulas below were employed to determine the effective density of states in the valence band (N_V) and conduction band (N_C) for double perovskite materials.[98]

$$N_C = \left(\frac{2\pi m_e k_B T}{\hbar^2}\right)^{3/2} \quad (22)$$

$$N_V = \left(\frac{2\pi m_h k_B T}{\hbar^2}\right)^{3/2} \quad (23)$$

In this equation, m_e and m_h denote the effective masses of electrons and holes, respectively, estimated from the band structure and DOS analyses. K_B is the Boltzmann constant (1.38×10^{-23} J K^{-1}), T is the temperature (typically 300 K), and $\hbar$ is Planck's constant (6.626×10^{-34} J s). Based on the band structure and DOS, the electron effective masses are 0.254 m_0 for Rb_2SnBr_6 and 0.271 m_0 for Rb_2PbCl_6, while the hole effective masses are 0.296 m_0 and 0.326 m_0, respectively. Table 5 lists the key simulation parameters for each functional layer.

The thickness of each layer is 50 nm for FTO and CdS, and 900 nm for both Rb_2SnBr_6 and Rb_2PbCl_6. The band gaps (E_g) are 3.6 eV for FTO, 2.42 eV for CdS, 1.451 eV for Rb_2SnBr_6, and 1.379 eV for Rb_2PbCl_6. The relative permittivity (ε_r) values are 10, 9.35, 3.71, and 3.46, respectively. The electron affinity (χ) ranges

Table 6 The simulated design of FTO/CdS/(Rb_2SnBr_6 and Rb_2PbCl_6) solar cells incorporates specific interface input parameters

Interfaces	Total defect density (cm^{-2})	Defect type	Capture cross section: electrons/holes (cm^2)
CdS/Rb_2SnBr_6	1×10^{11}	Neutral	1×10^{-19}
CdS/Rb_2PbCl_6	1×10^{11}	Neutral	1×10^{-19}

from 3.860 eV (Rb_2SnBr_6) to 4.910 eV (Rb_2PbCl_6). The conduction band effective density of states (N_C) is highest for Rb_2PbCl_6 (9.633×10^{18} cm^{-3}) and lowest for FTO (2×10^{18} cm^{-3}). The valence band effective density of states (N_V) follows a similar pattern, with 1.8×10^{19} cm^{-3} for FTO and CdS, 1.415×10^{19} cm^{-3} for Rb_2SnBr_6, and 1.741×10^{19} cm^{-3} for Rb_2PbCl_6. Regarding carrier concentrations, the shallow uniform acceptor density (N_A) is 1×10^{19} cm^{-3} for both Rb-based compounds, while it is zero for FTO and CdS. The shallow uniform donor density (N_D) is 1×10^{18} cm^{-3} for FTO, 1×10^{17} cm^{-3} for CdS, and zero for Rb_2SnBr_6 and Rb_2PbCl_6. Electron and hole thermal velocities are consistently 1×10^7 cm s^{-1} across all materials. The electron mobility (μ_n) is 50 cm^2 V^{-1} s^{-1} for FTO, 100 cm^2 V^{-1} s^{-1} for CdS and Rb-based compounds. Hole mobility (μ_h) varies from 20 cm^2 V^{-1} s^{-1} (FTO and Rb_2SnBr_6) to 50 cm^2 V^{-1} s^{-1} (Rb_2PbCl_6). Lastly, the total defect density is 1×10^{14} cm^{-3} for FTO, 1×10^{12} cm^{-3} for CdS, and 1×10^{13} cm^{-3} for both Rb_2SnBr_6 and Rb_2PbCl_6.

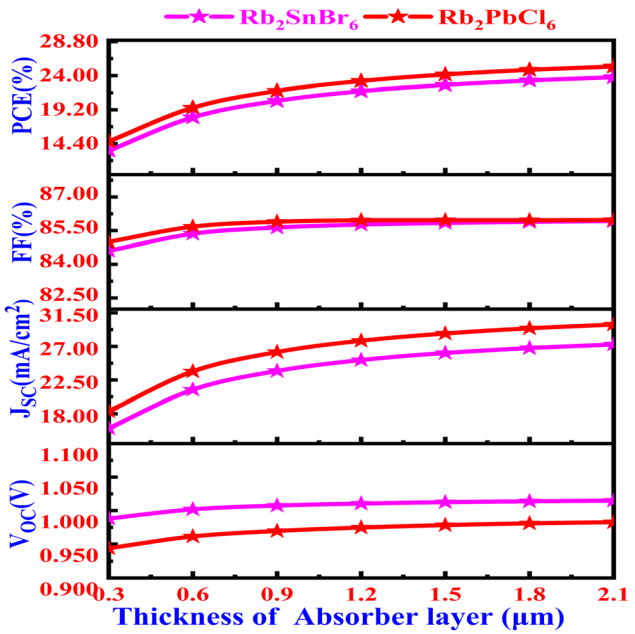

Fig. 11 Effect of variation in the thickness of absorber layer on Rb_2SnBr_6 and Rb_2PbCl_6 materials on PV parameters of V_{OC}, J_{SC}, FF, and PCE.

Table 6 summarizes the defect characteristics at the CdS/Rb_2SnBr_6 and CdS/Rb_2PbCl_6 interfaces. Both interfaces exhibit a total interface defect density of 1×10^{11} cm^{-2} and a neutral defect type. This value is not directly measured from experiments but is a commonly assumed moderate defect density for interface states in double perovskite solar cells, as used in previous simulation studies.[99,100] The capture cross-section for both electrons and holes (1×10^{-19} cm^2) at each interface was adopted from the standard SCAPS-1D default values,[99,101,102] which are widely used in modeling studies of perovskite-based devices. These assumptions provide a realistic representation of interfacial recombination processes in the absence of experimental data. The consistent values further indicate similar defect behavior at the two heterostructure interfaces.

3.9 Impact of thickness of absorber layer on inorganic Rb_2SnBr_6 and Rb_2PbCl_6 perovskites

Fig. 11 and Table 7 illustrate how varying the absorber layer thickness from 0.3 to 2.1 μm influences the photovoltaic performance of Rb_2SnBr_6 and Rb_2PbCl_6 absorber layers. Optimizing this thickness can greatly enhance the efficiency of thin-film solar cells.[103,104] The simulations were performed using SCAPS-1D. Optical absorption was treated under idealized conditions, assuming complete absorption within the specified layer thickness.[105] In contrast, the device simulations included finite defect densities, with a bulk defect density of 1×10^{13} cm^{-3} and an interface defect density of 1×10^{11} cm^{-2}, implemented as Shockley–Read–Hall recombination centers in SCAPS-1D. These parameters, together with those listed in Tables 5 and 6, govern the recombination processes and carrier dynamics in the devices. Under these conditions, increasing the absorber thickness enhances light absorption, particularly at longer wavelengths, thereby improving carrier generation and contributing to higher photovoltaic output.[106,107]

Table 7 Impact of absorber layer thickness on PV parameters of Rb_2SnBr_6 and Rb_2PbCl_6

Thickness of absorber layer	Rb_2SnBr_6				Rb_2PbCl_6			
	V_{OC} (V)	J_{SC} (mA cm^{-2})	FF (%)	PCE (%)	V_{OC} (V)	J_{SC} (mA cm^{-2})	FF (%)	PCE (%)
0.3	0.988	16.0361	84.596	13.4043	0.9437	18.324	84.995	14.698
0.6	1.001	21.18805	85.352	18.1159	0.961	23.636	85.671	19.467
0.9	1.007	23.69723	85.628	20.4388	0.969	26.227	85.891	21.838
1.2	1.010	25.15447	85.759	21.7960	0.974	27.737	85.953	23.236
1.5	1.012	26.1256	85.835	22.6798	0.978	28.721	85.960	24.151
1.8	1.013	26.76092	85.884	23.2992	0.980	29.410	85.960	24.796
2.1	1.014	27.24803	85.917	23.7564	0.982	29.919	85.966	25.274

However, not all parameters improve indefinitely. The investigation demonstrates that altering the absorber layer thickness has a moderate effect on V_{OC} and FF in Rb_2SnBr_6 and Rb_2PbCl_6 double perovskite structures. For both Rb_2SnBr_6 and Rb_2PbCl_6, the V_{OC} and FF increase up to approximately 0.9 μm, after which they plateau due to recombination balancing the photogenerated carrier density. As the absorber layer thickness increases, enhanced optical absorption, particularly at longer wavelengths, leads to an increase in the J_{SC}. This continues until approximately 1.5 μm, beyond which J_{SC} and the PCE begin to saturate due to the onset of absorption saturation and increased charge carrier recombination. Meanwhile, the V_{OC} and FF also improve initially but stabilize earlier, around 0.9 μm. These trends are consistent with previously reported studies that highlight the trade-offs between light absorption and recombination losses in thicker absorber layers.[79,103,104] However, V_{OC} and FF saturate at around 0.9 μm, while further increases in J_{SC} and PCE beyond this point show only marginal improvements. Therefore, 0.9 μm is considered the optimal absorber thickness. Beyond this threshold, additional thickness leads to higher material usage and fabrication costs without significant efficiency gains, making further expansion economically inefficient.

These findings align with prior simulation-based studies and provide an upper threshold beyond which increasing absorber thickness yields diminishing performance returns. The optimized efficiencies are 20.44% for Rb_2SnBr_6 and 21.84% for Rb_2PbCl_6, with Rb_2PbCl_6 exhibiting higher efficiency. However,

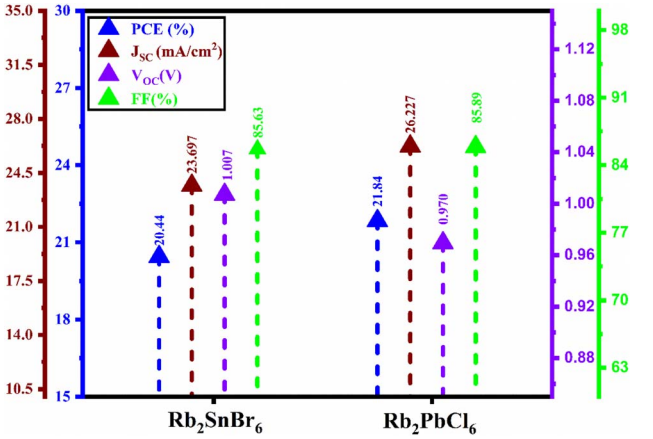

Fig. 13 Analysis of photovoltaic performance parameters in Rb_2SnBr_6 and Rb_2PbCl_6 perovskite materials.

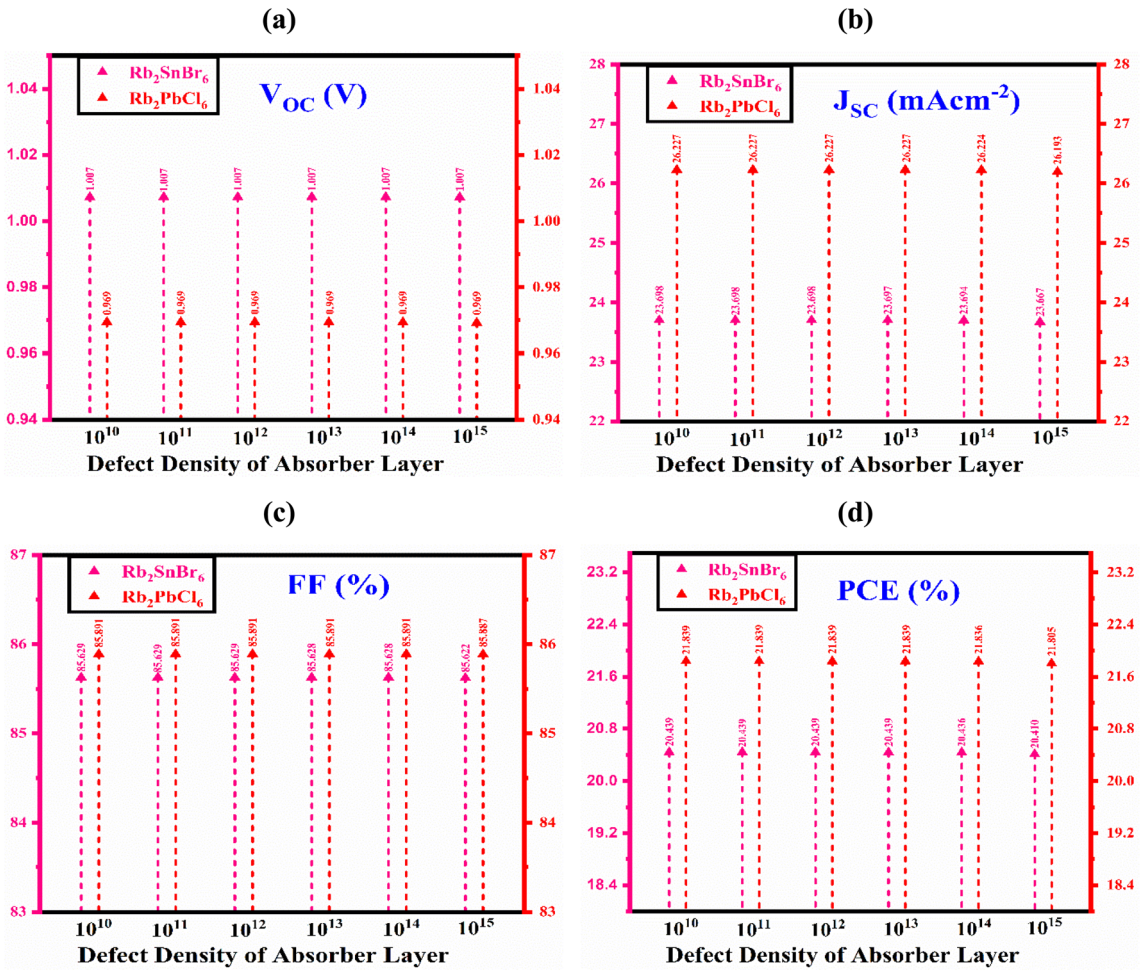

Fig. 12 Effects of defect density in the Rb_2SnBr_6 and Rb_2PbCl_6 absorber layer on PV parameters: (a) V_{OC}, (b) J_{SC}, (c) FF, and (d) PCE.

the presence of lead raises environmental concerns, making Rb_2SnBr_6 a preferable alternative as a lead-free material with promising potential for future solar cell applications.

3.10 Effect of defect density of the absorber layer in inorganic Rb_2SnBr_6 and Rb_2PbCl_6 perovskite materials

The performance of Al/FTO/CdS/(Rb_2BX_6 (Rb_2SnBr_6 and Rb_2PbCl_6))/Ni-structured Rb-based double perovskite solar cells is notably influenced by the defect density of the absorber layer, as depicted in Fig. 12a–d. This study examines defect density variations ranging from 10^{10} to 10^{15} cm^{-3} while keeping other material parameters constant. The findings reveal that V_{OC} remains relatively stable up to 10^{15} cm^{-3}, beyond which defect-induced recombination begins to degrade device performance. Meanwhile, J_{SC}, FF, and PCE show slight reductions with increasing defect density due to enhanced non-radiative recombination.

Notably, optimal performance is observed at a defect density of 10^{13} cm^{-3} for the CdS ETL layer, where Rb_2SnBr_6 achieves a V_{OC} of 1.007 V, J_{SC} of 23.697 mA cm^{-2}, FF of 85.628%, and PCE of 20.439%. In comparison, Rb_2PbCl_6 reaches a V_{OC} of 0.996 V, J_{SC} of 26.227 mA cm^{-2}, FF of 85.891%, and PCE = 21.893%. It is important to emphasize that these high FF values result from simulations under idealized conditions, assuming negligible interfacial recombination, optimal charge transport, and uniform material quality. While these values represent the theoretical performance limits, actual experimental devices may exhibit lower FF due to non-idealities. These results underscore the critical role of defect engineering in optimizing the efficiency of double perovskite solar cells.

3.11 Performance analysis of Rb-based double perovskite solar cells

Fig. 13 presents a comparative bar chart illustrating the photovoltaic performance parameters of Rb_2SnBr_6 and Rb_2PbCl_6 perovskite materials, including PCE, J_{SC}, V_{OC}, and FF. Each parameter is represented by a distinct color and symbol,

Table 8 Performance parameters of PV for Rb_2SnBr_6 and Rb_2PbCl_6, and various previous cell outlines

Structures	PCE (%)	J_{SC} (mA cm^{-2})	V_{OC} (volt)	FF (%)	References
Al/FTO/SnS_2/Ca_3NCl_3	8.54	7.044	1.378	88.10	108
Al/FTO/SnS_2/Sr_3NCl_3	18.11	16.786	1.248	86.44	108
Al/FTO/CdS/Ba_3NCl_3/Au	32.00	38.21	1.036	80.75	109
Al/FTO/CdS/Rb_2SnBr_6/Ni	20.44	26.697	1.0073	85.63	This work
Al/FTO/CdS/Rb_2PbCl_6/Ni	21.84	26.227	0.9695	85.89	This work

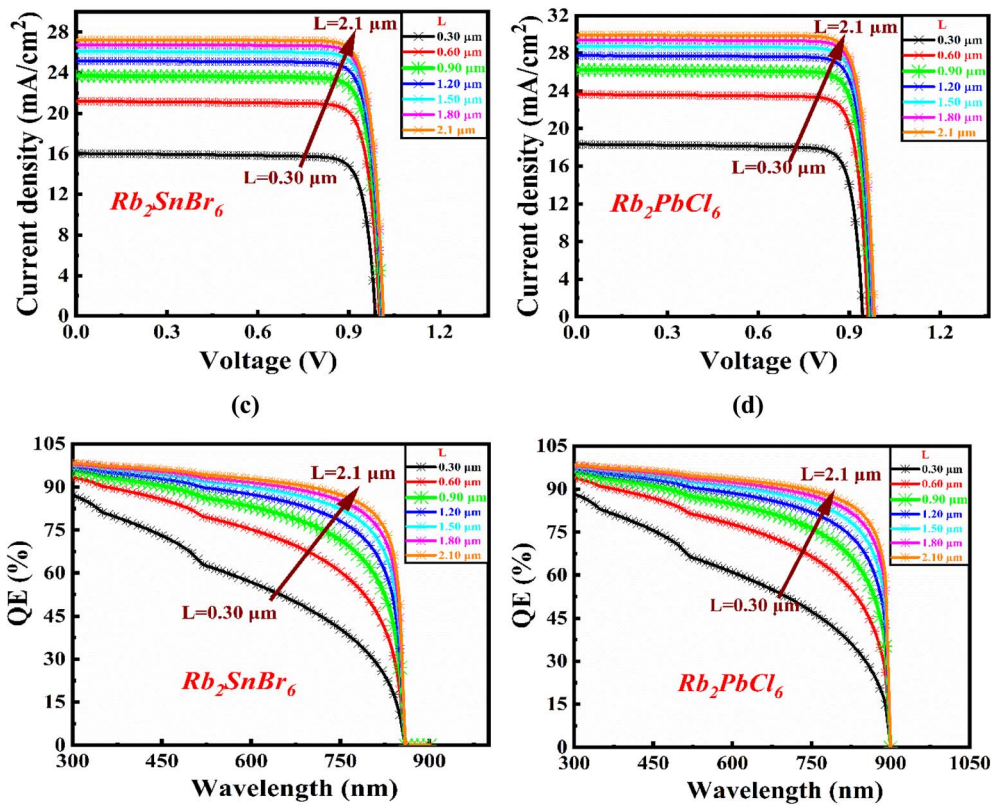

Fig. 14 (a and c) J–V characteristics, and (b and d) Q–E response for Rb_2SnBr_6 and Rb_2PbCl_6 materials.

ensuring clear differentiation. The results indicate that Rb_2SnBr_6 achieves a PCE of 20.44%, J_{SC} of 23.697 mA cm^{-2}, V_{OC} of 1.007 V, and an FF of 85.63%.

In comparison, Rb_2PbCl_6 exhibits slightly higher values for PCE (21.84%) and J_{SC} (26.227 mA cm^{-2}) but a lower V_{OC} (0.970 V), while maintaining a similar FF (85.89%). The left *y*-axis represents PCE and J_{SC}, whereas the right *y*-axis corresponds to V_{OC} and FF, allowing a clear visualization of the performance trends. Although Rb_2PbCl_6 demonstrates superior photovoltaic performance with higher PCE and J_{SC}, its lead content poses significant environmental and toxicity concerns. On the other hand, Rb_2SnBr_6, despite its slightly lower efficiency, offers a lead-free and environmentally safer alternative. Given the increasing focus on sustainable and non-toxic materials for solar energy applications, Rb_2SnBr_6 emerges as a promising candidate for future solar cell development, striking a balance between performance and environmental responsibility.

Table 8 compares the performance parameters of photovoltaic (PV) cells for Rb_2SnBr_6 and Rb_2PbCl_6 with previously reported cell structures. Table 8 presents key metrics including PCE, J_{SC}, FF, and V_{OC}.

The cells reported in this work include the Al/FTO/CdS/Rb_2SnBr_6/Ni structure, which achieved a PCE of 20.44%, a J_{SC} of 26.697 mA cm^{-2}, V_{OC} of 1.0073 V, and FF of 85.63%, and the Al/FTO/CdS/Rb_2PbCl_6/Ni structure, which showed a PCE of 21.84%, J_{SC} of 26.227 mA cm^{-2}, VOC of 0.9695 V, and FF of 85.89%. These results are competitive when compared to earlier reported structures, such as Al/FTO/SnS_2/Ca_3NCl_3 with a PCE of 8.54% and Al/FTO/CdS/Ba_3NCl_3/Au with a PCE of 32.00%.

3.12 *J–V* and *Q–E* properties of Rb_2SnBr_6 and Rb_2PbCl_6 materials

Fig. 14a–d presents the current density–voltage (*J–V*) and quantum efficiency (*Q–E*) curves for the optimized solar cell structure (Al/FTO/CdS/Rb_2SnBr_6 and Rb_2PbCl_6/Ni), highlighting the impact of absorber layer thickness variations from 0.30 μm to 2.1 μm on device performance. Both Rb_2SnBr_6 and Rb_2PbCl_6 exhibit strong potential as absorber materials.

The thickness of the absorber layer significantly influences the *J–V* and *Q–E* characteristics of the solar cell. Increasing the absorber thickness enhances J_{SC} due to improved light absorption and higher photocurrent generation. However, while thicker layers enhance absorption, they may also lead to increased recombination losses, potentially reducing V_{OC}, FF, and overall efficiency.

4 Conclusion

This study systematically explores the structural, electronic, optical, mechanical, and photovoltaic properties of Rb_2BX_6 (B = Sn, Pb; X = Cl, Br) double halide perovskites using DFT calculations and SCAPS-1D simulations. The negative formation energies confirm their thermodynamic stability, while the Born stability criteria validate their mechanical robustness. Among them, Rb_2SnCl_6 exhibits the highest tolerance factor (0.9672), ensuring structural stability, whereas Rb_2SnBr_6 (0.9526) shows a slight reduction due to the larger Br^- ion. Mechanical analysis reveals that Rb_2SnBr_6 is highly ductile, with a Poisson's ratio of 0.393 and Pugh's ratio of 4.342, whereas Rb_2PbCl_6 is brittle, with values of 0.188 and 1.272. Electronic structure calculations confirm that Rb_2SnBr_6 and Rb_2PbCl_6 are direct bandgap semiconductors with band gaps of 1.451 eV and 1.379 eV, respectively. DOS analysis highlights that the valence band is mainly derived from Sn-5s/Pb-6s and halogen states, while the conduction band is dominated by Rb-4p states. These compounds exhibit strong visible-light absorption, making them promising candidates for solar cell applications. Rb_2SnCl_6 and Rb_2PbCl_6 are dynamically stable, whereas Rb_2SnBr_6 and Rb_2PbBr_6 exhibit dynamic instability. To evaluate photovoltaic performance, SCAPS-1D simulations were performed, identifying an optimal absorber thickness of 900 nm and a defect density of 10^{13} cm^{-3}. Under these conditions, the predicted PCEs of Rb_2SnBr_6 and Rb_2PbCl_6 are 20.44% and 21.84%, respectively, with corresponding FF values of 85.63% and 85.89%, J_{SC} of 26.697 and 26.227 mA cm^{-2}, and V_{OC} of 1.0073 and 0.9695 V. Both compounds exhibit excellent photovoltaic performance. While Rb_2PbCl_6 delivers slightly higher efficiency, its mechanical brittleness and toxic lead content raise sustainability concerns. In contrast, Rb_2SnBr_6 provides a lead-free alternative with favorable optoelectronic properties and enhanced mechanical flexibility, but dynamic instability, making it a strong candidate for next-generation perovskite solar cells and energy harvesting applications.

Ethical statement

The manuscript's authors agree that there are no research involving human participants, human data or tissue, or animal subjects.

Author contributions

Imtiaz Ahamed Apon, Md. Azizur Rahman, Md. Alamgir Hossain: methodology, validation, software, conceptualization, investigation, formal analysis, data curation, visualization, writing – original draft, and review and editing. Karim KRIAA, Chemseddine Maatki, Amine Aymen Assadi, Noureddine Elboughdiri: investigation, validation, software, formal analysis, data curation, writing – original draft, and review and editing.

Conflicts of interest

The authors have no conflicts of interest.

Data availability

Data will be made available on reasonable request.

Funding statement

This work was supported and funded by the Deanship of Scientific Research at Imam Mohammad Ibn Saud Islamic University (IMSIU) (grant number IMSIU-DDRSP2502).

References

1 B. Cucco, G. Bouder, L. Pedesseau, C. Katan, J. Even, M. Kepenekian and G. Volonakis, *Appl. Phys. Lett.*, 2021, **119**, 181903.
2 Y. Cai, W. Xie, H. Ding, Y. Chen, K. Thirumal, L. H. Wong, N. Mathews, S. G. Mhaisalkar, M. Sherburne and M. Asta, *Chem. Mater.*, 2017, **29**, 7740–7749.
3 L. Ortega-San-Martin, in *Revolution of Perovskite*, ed. N. S. Arul and V. D. Nithya, Springer Singapore, Singapore, 2020, pp. 1–41.
4 A. Kojima, K. Teshima, Y. Shirai and T. Miyasaka, *J. Am. Chem. Soc.*, 2009, **131**, 6050–6051.
5 N. K. Noel, A. Abate, S. D. Stranks, E. S. Parrott, V. M. Burlakov, A. Goriely and H. J. Snaith, *ACS Nano*, 2014, **8**, 9815–9821.
6 Q. Mahmood, M. H. Alhossainy, M. S. Rashid, T. H. Flemban, H. Althib, T. Alshahrani, M. Rashid and A. Laref, *J. Mater. Sci. Eng. B*, 2021, **266**, 115064.
7 H. Habib, M. Haleem, M. Rashid, A. Ali, A. S. Bhatti, Z. Ali and M. Hussain, *J. Comput. Electron.*, 2024, **23**, 1262–1283.
8 Q. Mahmood, M. Younas, M. G. B. Ashiq, S. M. Ramay, A. Mahmood and H. M. Ghaithan, *Int. J. Energy Res.*, 2021, **45**, 14995–15004.
9 M. Singh, Akash and J. P. Tiwari, *ACS Appl. Energy Mater.*, 2024, **7**, 10212–10229.
10 S. Mehra, Mamta, J. Tawale, G. Gupta, V. N. Singh, A. K. Srivastava and S. N. Sharma, *Heliyon*, 2024, **10**, e33243.
11 Y. Zhang, S.-G. Kim, D. Lee, H. Shin and N.-G. Park, *Energy Environ. Sci.*, 2019, **12**, 308–321.
12 X. Li, Y. Wu, S. Zhang, B. Cai, Y. Gu, J. Song and H. Zeng, *Adv. Funct. Mater.*, 2016, **26**, 2435–2445.
13 Y.-L. Yu, W.-Y. Yang, A. Hara, K. Asayama, H. A. Roels, T. S. Nawrot and J. A. Staessen, *Hypertens. Res.*, 2023, **46**, 395–407.
14 K. J. Savill, A. M. Ulatowski and L. M. Herz, *ACS Energy Lett.*, 2021, **6**, 2413–2426.
15 R. K. Pingak, A. Harbi, S. Bouhmaidi, A. Z. Johannes, N. U. J. Hauwali, W. Khan, F. Nitti, D. Tambaru, M. Moutaabbid and L. Setti, *Chem. Phys. Impact*, 2024, **9**, 100749.
16 C. J. Bennett, H. E. A. Brand, A. K. L. Yuen, M. K. Nicholas and B. J. Kennedy, *J. Solid State Chem.*, 2024, **329**, 124427.
17 M. Khuili, A. Ouhammou, N. Fazouan, E. H. Atmani, I. Allaoui, S. Al-Qaisi, K. Maher and R. Bouidmar, *Mod. Phys. Lett. B*, 2024, **38**, 2350223.
18 M. Faizan, K. C. Bhamu, G. Murtaza, X. He, N. Kulhari, M. M. AL-Anazy and S. H. Khan, *Sci. Rep.*, 2021, **11**, 6965.
19 M. M. S. Karim, A. M. Ganose, L. Pieters, W. W. Winnie Leung, J. Wade, L. Zhang, D. O. Scanlon and R. G. Palgrave, *Chem. Mater.*, 2019, **31**, 9430–9444.
20 K. Vamsi Krishna, S. Sritanvi, N. Reddy, S. Reddy, D. Nandyala, A. Pandarinath, G. Nagakumari, R. Mahesh, P. Venugopal Reddy and V. Kandrapu, in *Organic and Hybrid Light Emitting Materials and Devices XXVI*, ed. T.-W. Lee, F. So and C. Adachi, SPIE, San Diego, United States, 2022, p. 60.
21 R. Hasan, H. Z. Aslam, R. Joshi, R. A. Lalancette and G. Akopov, *Dalton Trans.*, 2025, **54**, 3796–3803.
22 K. Bouferrache, M. A. Ghebouli, B. Ghebouli, M. A. Habila, T. Chihi, M. Fatmi, A. Djemli and M. Sillanpaa, *Results Phys.*, 2024, **56**, 107138.
23 R. Rafiu, Md. S. Hasan Saikot, A. El-Rayyes, I. A. Apon, M. Shkir, M. T. Khan, M. A. Sayed and Md. A. Rahman, *J. Phys. Chem. Solids*, 2026, **208**, 113126.
24 Md. S. H. Saikot, R. Rafiu, I. Boukris, Md. A. Rahman, I. A. Apon, R. Kawsar, M. T. Khan, H. Etabti, J. Rajabathar and H. Albalawi, *New J. Chem.*, 2025, **49**(39), 17221–17245.
25 M. C. Payne, M. P. Teter, D. C. Allan, T. A. Arias and J. D. Joannopoulos, *Rev. Mod. Phys.*, 1992, **64**, 1045–1097.
26 S. J. Clark, M. D. Segall, C. J. Pickard, P. J. Hasnip, M. I. J. Probert, K. Refson and M. C. Payne, *Z. Kristallogr. Cryst. Mater.*, 2005, **220**, 567–570.
27 K. Momma and F. Izumi, *J. Appl. Crystallogr.*, 2011, **44**, 1272–1276.
28 H. J. Monkhorst and J. D. Pack, *Phys. Rev. B*, 1976, **13**, 5188–5192.
29 J. P. Perdew, K. Burke and M. Ernzerhof, *Phys. Rev. Lett.*, 1996, **77**, 3865–3868.
30 A. D. Becke, *Phys. Rev. A*, 1988, **38**, 3098–3100.
31 C. Lee, W. Yang and R. G. Parr, *Phys. Rev. B: Condens. Matter Mater. Phys.*, 1988, **37**, 785–789.
32 R. Gaillac, P. Pullumbi and F.-X. Coudert, *J. Phys.: Condens. Matter*, 2016, **28**, 275201.
33 C. Fonseca Guerra, J. Handgraaf, E. J. Baerends and F. M. Bickelhaupt, *J. Comput. Chem.*, 2004, **25**, 189–210.
34 J. Verschraegen and M. Burgelman, *Thin Solid Films*, 2007, **515**, 6276–6279.
35 M. Burgelman, P. Nollet and S. Degrave, *Thin Solid Films*, 2000, **361–362**, 527–532.
36 Md. A. Rahman, A. Ghosh, R. J. Ramalingam, N. Elboughdiri, A. M. Alsuhaibani, Q. Mohsen, M. S. Refat and I. A. Apon, *Opt. Commun.*, 2025, 131873.
37 K. Chakraborty, M. G. Choudhury and S. Paul, *Sol. Energy*, 2019, **194**, 886–892.
38 L. Chen, in *Proceedings of the 4th International Conference on Art Studies: Science, Experience, Education (ICASSEE 2020)*, Atlantis Press, Moscow, Russia, 2020.
39 W. Rahim, A. Cheng, C. Lyu, T. Shi, Z. Wang, D. O. Scanlon and R. G. Palgrave, *Chem. Mater.*, 2020, **32**, 9573–9583.
40 X. Diao, Y. Diao, Y. Tang, G. Zhao, Q. Gu, Y. Xie, Y. Shi, P. Zhu and L. Zhang, *Sci. Rep.*, 2022, **12**, 12633.
41 M. A. Ali, A. A. A. Bahajjaj, S. Al-Qaisi, M. Sillanpää, A. Khan and X. Wang, *J. Comput. Chem.*, 2023, **44**, 1875–1883.
42 P. Hohenberg and W. Kohn, *Phys. Rev.*, 1964, **136**, B864.
43 F. D. Murnaghan, *Am. J. Math.*, 1937, **59**, 235–260.
44 J. M. Skelton, D. Tiana, S. C. Parker, A. Togo, I. Tanaka and A. Walsh, *J. Chem. Phys.*, 2015, **143**, 064710.
45 S. Park, B. Lee, S. H. Jeon and S. Han, *J. Mater. Chem. C*, 2011, **11**, S337–S340.
46 M. M. H. Babu, T. Saha, J. Podder, P. Roy, A. Barik and E. Haque, *Heliyon*, 2021, **7**, e07796.

47 K. Oukacha, L. Laânab, M. A. Bossi, S. E. Hajjaji and B. Jaber, *J. Inorg. Organomet. Polym. Mater.*, 2025, DOI: 10.1007/s10904-025-03871-9.
48 R. K. Pingak, A. Harbi, F. Nitti, S. Bouhmaidi, D. Tambaru, A. Z. Johannes, N. U. J. Hauwali, A. Wahid, M. Moutaabbid and L. Setti, *Mater. Sci. Semicond. Process.*, 2025, **186**, 109044.
49 Z. Khan, A. Manan, N. U. Khan, H. A. Althobaiti, A. N. Khan, A. Khan and G. Liu, *Chem. Pap.*, 2025, **79**(11), 7657–7677.
50 D. M. Adams and A. J. Norman, *J. Phys.: Condens. Matter*, 1991, **3**, 3211–3214.
51 A. Kaltzoglou, M. Antoniadou, A. G. Kontos, C. C. Stoumpos, D. Perganti, E. Siranidi, V. Raptis, K. Trohidou, V. Psycharis, M. G. Kanatzidis and P. Falaras, *J. Phys. Chem. C*, 2016, **120**, 11777–11785.
52 R. Rafiu, M. S. H. Saikot, A. El-Rayyes, I. A. Apon, M. Shkir, M. T. Khan, M. A. Sayed and M. A. Rahman, *J. Phys. Chem. Solids*, 2026, **208**, 113126.
53 T. B. Brill, R. C. Gearhart and W. A. Welsh, *J. Magn. Reson.*, 1974, **13**, 27–37.
54 S. Burger, M. G. Ehrenreich and G. Kieslich, *J. Mater. Chem. A*, 2018, **6**, 21785–21793.
55 U.-G. Jong, C.-J. Yu and Y.-H. Kye, *RSC Adv.*, 2020, **10**, 201–209.
56 Md. Harun-Or-Rashid, L. B. Farhat, A. Brahmia, M. K. A. Mohammed, Md. A. Rahman, A. Azzouz-Rached and Md. F. Rahman, *J. Mater. Sci.*, 2024, **59**, 6365–6385.
57 M. Afsuddin, M. M. Hasan and M. L. Ali, *J. Inorg. Organomet. Polym. Mater.*, 2024, **690**, 416203.
58 M. Ahmed, A. Bakar, A. Quader, R. Ahmad and S. Ramay, *Chem. Phys.*, 2024, **581**, 112260.
59 A. Hachani, A. Mahammedi, M. Rougab, A. Gueddouh and M. L. Belkhir, *Chem. Phys.*, 2025, **598**, 112833.
60 Md. A. Rahman, Md. F. Rahman, Md. H. Rahman, Md. R. Islam and M. Z. Bani-Fwaz, *Appl. Phys. Lett.*, 2024, **125**, 193902.
61 L. Benahmedi, A. Besbes and R. Djelti, *Mater. Chem. Phys.*, 2025, **334**, 130520.
62 A. Kopp, J. Werner, N. Kröger, T. E. Weirich and F. D'Elia, *Biomater. Adv.*, 2024, **157**, 213756.
63 R. Hill, *Proc. Phys. Soc., London, Sect. A*, 1952, **65**, 349.
64 M. M. Rahaman, M. H. K. Rubel, M. A. Rashid, M. A. Alam, K. M. Hossain, M. I. Hossain, A. A. Khatun, M. M. Hossain, A. K. M. A. Islam, S. Kojima and N. Kumada, *J. Mater. Res. Technol.*, 2019, **8**, 3783–3794.
65 M. F. Rahman, P. Barman, M. A. Rahman, M. Mushtaq, M. R. Islam, M. A. Rahman, M. Z. Sultan, A. R. Chaudhry and A. Irfan, *Polyhedron*, 2024, **254**, 116937.
66 R. K. Pingak, A. Harbi, F. Nitti, S. Bouhmaidi, D. Tambaru, A. Z. Johannes, N. U. J. Hauwali, A. Wahid, M. Moutaabbid and L. Setti, *Mater. Sci. Semicond. Process.*, 2025, **186**, 109044.
67 R. Hasan, H. Z. Aslam, R. Joshi, R. A. Lalancette and G. Akopov, *Dalton Trans.*, 2025, **54**, 3796–3803.
68 M. H. Rahman, F. Ahmed, N. Elboughdiri, K. KRIAA, M. S. Uddin, M. A. Rahman, M. N. Tasnim, I. Boukhris, A. Akremi, J. R. Rajabathar and M. T. Khan, *Polyhedron*, 2025, **280**, 117676.
69 M. S. I. Ria, Md. A. Rahman, A. Ghosh, M. M. Billah, D. Das, N. Elboughdiri, A. M. Alsuhaibani, Q. Mohsen, M. S. Refat, I. Boukris and M. T. Khan, *J. Phys. Chem. Solids*, 2025, 112955.
70 A. Crovetto, R. Chen, R. B. Ettlinger, A. C. Cazzaniga, J. Schou, C. Persson and O. Hansen, *Sol. Energy Mater. Sol. Cells*, 2016, **154**, 121–129.
71 C. Ambrosch-Draxl and J. O. Sofo, *Comput. Phys. Commun.*, 2006, **175**, 1–14.
72 G. Nazir, A. Ahmad, M. F. Khan and S. Tariq, *Comput. Condens. Matter*, 2015, **4**, 32–39.
73 M. Usman Ghani, M. Sagir, M. Bilal Tahir, H. I. Elsaeedy, S. Nazir, H. Alrobei and M. Alzaid, *Inorg. Chem. Commun.*, 2023, **155**, 111007.
74 O. D. Iakobson, O. L. Gribkova, A. R. Tameev and J.-M. Nunzi, *Sci. Rep.*, 2021, **11**, 5005.
75 P. Mondal, N. A. Shahed, S. Khanom, M. K. Hossain and F. Ahmed, *Mater. Chem. Phys.*, 2022, **277**, 125429.
76 M. R. Hasan, I. A. Apon and Md. Alamgir Hossain, *AIP Adv.*, 2025, **15**, 035032.
77 M. D. Ratul Hasan, I. A. Apon, I. Ahmed Ovi and F.-T. -Zahra, *Int. J. Energy Res.*, 2024, **2024**, 8213804.
78 C. N. Pace, F. Vajdos, L. Fee, G. Grimsley and T. Gray, *Protein Sci.*, 1995, **4**, 2411–2423.
79 M. A. Rahman, A. Ghosh, N. S. Awwad, N. Elboughdiri, A. M. Alsuhaibani, Q. Mohsen and M. S. Refat, *J. Phys. Chem. Solids*, 2025, **203**, 112728.
80 M. Fox and G. F. Bertsch, *Am. J. Phys.*, 2002, **70**, 1269–1270.
81 P. Sharma and R. K. Mishra, *J. Renew. Sustain. Energy.*, 2025, **14**, 21.
82 Y. Wang, J. Lv, L. Zhu and Y. Ma, *Comput. Phys. Commun.*, 2012, **183**, 2063–2070.
83 W. Shockley and H. J. Queisser, *J. Appl. Phys.*, 1961, **32**, 510–519.
84 C.-S. Man and M. Huang, *J. Thermoelasticity*, 2011, **105**, 29–48.
85 S. I. Ranganathan and M. Ostoja-Starzewski, *Phys. Rev. Lett.*, 2008, **101**, 055504.
86 I. A. Apon, Md. R. Hasan and M. Islam, *Phys. Scr.*, 2025, **100**, 015931.
87 Md. R. Hasan, I. A. Apon, Md. M. Islam, A. U. Azad, Md. Aminuzzman and Md. S. Haque, *AIP Adv.*, 2024, **14**, 115109.
88 C.-J. Yu, I.-C. Ri, H.-M. Ri, J.-H. Jang, Y.-S. Kim and U.-G. Jong, *RSC Adv.*, 2023, **13**, 16012–16022.
89 M. S. Reza, M. F. Rahman, A. Kuddus, M. K. A. Mohammed, A. K. Al-Mousoi, M. R. Islam, A. Ghosh, S. Bhattarai, R. Pandey, J. Madan and M. K. Hossain, *RSC Adv.*, 2023, **13**, 31330–31345.
90 S. M. A. Al Hussan, N. A. Bakr, A. N. Abd and M. A. Khalaf, *J. Ovonic Res.*, 2021, **17**, 395–403.
91 F. Sadegh, E. Akman, D. Prochowicz, M. M. Tavakoli, P. Yadav and S. Akin, *ACS Appl. Mater. Interfaces*, 2022, **14**, 38631–38641.

92 M. Z. Arif, Md. Z. Alam, N. K. Chowdhury, A. Dutta and S. Baruri, *Mathematics and Engineering Technologies (iCoMET)*, 2023, 1–6.
93 S. Wei and A. Zunger, *J. Appl. Phys.*, 1995, **78**, 3846–3856.
94 M. Gajdoıfmmode, K. Hummer, G. Kresse, J. Furthmüller and F. Bechstedt, *Phys. Rev. B: Condens. Matter Mater. Phys.*, 2006, **73**, 045112.
95 W. S. Lau, D. S. H. Chan, J. C. H. Phang, K. W. Chow, K. S. Pey, Y. P. Lim, B. Cronquist, *Appl. Phys. Lett.*, 1993, 63, pp. 5–75.
96 J. Kang and L.-W. Wang, *J. Phys. Chem. Lett.*, 2017, **8**(2), 489–493.
97 C. Motta, F. El-Mellouhi and S. Sanvito, *Sci. Rep.*, 2015, **5**, 12746.
98 S. M. Sze and K. K. Ng, *Physics of Semiconductor Devices*, 2006, 5–75, DOI: **10.1002/0470068329**.
99 I. A. Apon, M. A. Hossain, R. Rafiu, M. S. H. Saikot, M. A. Rahman, J. R. Rajabathar, I. Boukhris, H. Albalawi, K. Kriaa, N. Elboughdiri, *J. Inorg. Organomet. Polym. Mater.*, 2025, 717, pp. 1–6.
100 R. Rafiu, M. S. H. Saikot, A. El-Rayyes, I. A. Apon, M. Shkir, M. T. Khan, M. A. Sayed and M. A. Rahman, *J. Phys. Chem. Solids*, 2026, **208**, 113126.
101 R. Rafiu, Md. S. Hasan Saikot, I. A. Apon, I. Boukhris, A. El-Rayyes, M. T. Khan, Q. Mohsen and Md. A. Rahman, *J. Comput. Chem.*, 2025, **46**, e70221.
102 T. A. Chowdhury, *Opt. Continuum*, 2024, **3**, 1341–1368.
103 M. S. Reza, A. Ghosh, S. N. Wornob, M. S. Reza, A. K. Azad, M. M. Hossain, N. S. Awwad and H. A. Ibrahium, *J. Phys. Chem. Solids*, 2024, **194**, 112250.
104 A. Ghosh, M. S. Islam, M. K. Rahman, M. F. I. Buian, A. A. Hassan, H. A. Alrafai and S. K. A. Abdelrahim, *J. Mater. Sci. Eng. B*, 2024, **307**, 117521.
105 N. Elboughdiri, B. B. Sarkar, Md. A. Rahman, A. M. A. Adam, Md. H. Rahman, J. R. Rajabathar, Q. Mohsen, A. A. Alshihri, M. T. Khan, Md. S. Uddin and S. Saidi, *New J. Chem.*, 2025, **49**, 14529–14552.
106 O. A. M. Abdelraouf and N. K. Allam, *Opt. Mater.*, 2016, **54**, 84–88.
107 M. Burgelman, P. Nollet and S. Degrave, *Thin Solid Films*, 2000, **361–362**, 527–532.
108 Md. A. Rahman, Md. F. Rahman, L. Marasamy, Md. Harun-Or-Rashid, A. Ghosh, A. R. Chaudhry and A. Irfan, *Energy Fuels*, 2024, **38**(9), 8199–8217.
109 A. Hassan, S. Ria, A. Ghosh, H. Alrafai, A. Baki, S. Abdelrahim, J. Al-Humaid, R. Rabin, M. Rahman and M. Maniruzzaman, *J. Mater. Sci. Eng. B*, 2024, **308**, 117559.